Surface & Coatings Technology 476 (2024) 130270

Contents lists available at ScienceDirect

Surface & Coatings Technology

journal homepage: www.elsevier.com/locate/surfcoat

The effect of ceramic YSZ powder morphology on coating performance for industrial TBCs

Simone Bursich [a], Stefania Morelli [b,*], Giovanni Bolelli [b,c,d], Greta Cavazzini [a], Edoardo Rossi [e], Francesco Gerardo Mecca [b], Salvatore Petruzzi [b], Edoardo Bemporad [e], Luca Lusvarghi [b,c,d]

[a] Lincotek Rubbiano S.p.A. - Surface Solutions Division, Via Mistrali 7, 43046 Rubbiano di Solignano (PR), Italy
[b] Department of Engineering "Enzo Ferrari", Università di Modena e Reggio Emilia, Via Pietro Vivarelli 10/1, 41125 Modena (MO), Italy
[c] InterMech – MO.RE. Centro Interdipartimentale per la Ricerca Applicata e i Servizi nel Settore della Meccanica Avanzata e della Motoristica, Università di Modena e Reggio Emilia, Via Pietro Vivarelli 2, 41125 Modena (MO), Italy
[d] Consorzio Interuniversitario Nazionale per la Scienza e Tecnologia dei Materiali (INSTM), Local Unit: Università di Modena e Reggio Emilia, Via Pietro Vivarelli 10/1, 41125 Modena (MO), Italy
[e] Università degli studi Roma Tre, Department of Civil, Computer and Aeronautical Engineering, Via Vito Volterra 62, 00146 Rome, Italy

ARTICLE INFO

Keywords:
Thermal barrier coating (TBC)
CMAS corrosion
Thermal cycling fatigue
ZrO_2–55wt%Y_2O_3
Multilayer coatings
Dense vertically cracked (DVC) coatings

ABSTRACT

The increasing turbine inlet temperatures in modern gas turbines have raised concerns about the corrosion of ceramic thermal barrier coatings (TBCs) caused by molten silicate deposits, commonly referred to as "CMAS" due to their main constituents (CaO-MgO-Al_2O_3-SiO_2). The objective of this study was to investigate the combined influence of powder morphology and chemical composition on the CMAS resistance and thermal cycling resistance of ceramic monolayer and bi-layer coatings created through Atmospheric Plasma Spraying (APS). Three powder morphologies were examined: porous Agglomerated and Sintered (A&S) granules, Hollow Spherical (HOSP) powders, and dense, irregular Fused and Crushed (F&C) particles. Monolayer 7-8YSZ coatings with both porous and dense vertically cracked (DVC) microstructures, and bi-layer coatings consisting of a bottom layer of porous standard 7-8YSZ and a top layer composed of a porous high-yttrium ZrO_2–55 wt% Y_2O_3 were obtained using all three powder types (A&S, HOSP, or F&C). Furthermore, the bi-layer systems were deposited with different ratios between the individual layer thicknesses and/or different total thickness. FEG-SEM, EDX, and micro-Raman analyses, were conducted to assess the coatings' performance. Nanoindentation high-speed mapping and pillar splitting test were performed to evaluate the mechanical behaviour. The study on 8YSZ monolayers shows that coatings from a F&C feedstock exhibit higher density, reducing the CMAS penetration. However, these coatings demonstrate poorer thermal cycling performance due to increased stiffness and thermal stresses. Coatings from HOSP and A&S powders allow CMAS penetration but offer stress relief pathways, enhancing the coating's ability to withstand thermal stresses. Bi-layer coatings with a 55YSZ top coat show superior CMAS resistance compared to 7-8YSZ monolayer coatings, with limited penetration causing top coat peeling. The thickness ratio between the layers also affects thermal cycling resistance, where a thinner 55YSZ layer extends the TBC lifetime.

1. Introduction

Thermal Barrier Coatings (TBCs) are complex, multi-layer systems of various materials used to protect hot metallic components in turbines and engines for aviation and power generation from the damaging effects of hot gases [1,2]. These systems and cooling systems are designed to lower the surface temperature of components such as high-pressure turbine blades and vanes [3]. By using TBCs, it has been shown that the temperature can be reduced by as much as 300 °C [4]. The traditional TBC system consists of a metallic bond coat, such as an MCrAlY alloy (where M usually means Ni, Co or a combination of both), which provides protection against oxidation and enhances the adhesion of the top coat; a thermally grown oxide (TGO); and a ceramic top coat that offers thermal insulation for the metal components. Currently, the top-performing ceramic top coat is 7–8 wt% Yttria-stabilized Zirconia (YSZ) due to its low thermal conductivity and high melting point of

* Corresponding author.
E-mail address: stefania.morelli@unimore.it (S. Morelli).

https://doi.org/10.1016/j.surfcoat.2023.130270
Received 4 October 2023; Received in revised form 23 November 2023; Accepted 29 November 2023
Available online 4 December 2023

2690 °C [5]. However, the pursuit of greater gas turbine efficiency has led to a rise in inlet temperatures, exceeding 1200 °C [3]. This has also brought about the emergence of two significant issues. One is the corrosion caused by siliceous debris known as CMAS (CaO, MgO, Al_2O_3, and SiO_2) contained in dust-filled environments [6–8]. The CMAS debris melts at such high temperatures; therefore, when the molten particles hit the TBC surface, they form a liquid deposit that infiltrates into the YSZ TBC itself. The filling of the voids by molten CMAS followed by solidification during cooling leads to the ceramic top coat stiffening. This, in turn, compromises its elastic compliance and renders it susceptible to spalling during thermal cycling.

On the other hand, molten CMAS can chemically react with YSZ. CMAS dissolves yttria-stabilized zirconia, which can be followed by the re-precipitation of zirconia depleted of yttria. When this happens, the high-temperature tetragonal phase of yttria-depleted zirconia turns into a monoclinic phase during cooling. This is accompanied by a significant volume change (4 vol%), which causes coating spallation. Finally, even in the absence of CMAS deposits, the spontaneous transformation from the t' phase to the stable tetragonal and cubic (t and c) phases in 7-8YSZ is accelerated at temperatures above 1200 °C [9].

Therefore, in recent years, much research has been conducted to improve the durability of TBCs, using alternative materials to 7-8YSZ (zirconia doped with different rare-earth (RE) cations, pyrochlores, perovskites and hexaaluminates) [6,10–12], varying the TBC's microstructure (from traditional porous to dense, vertically cracked coatings), or employing different architectures (from single layers to multilayers) [13–15].

In this context, a possible alternative to traditional 7-8YSZ is zirconia stabilized with a high yttria content (fully stabilized zirconia, i.e., with a thermodynamically stable cubic phase over the entire temperature range up to the melting point) [16]. Few studies reported on the CMAS corrosion and thermal cycling resistance of TBCs with a higher content of yttria [17,18]. Juan et al. established a critical threshold of yttria content beyond which the coating is protected against CMAS penetration. They pointed out that a minimum amount of $50YO_{1.5}$ (mol.%) is required to promote the formation of the Y-apatite phase when in contact with a CMAS melt, which has a sealing effect on the coating [18]. One disadvantage of the fully stabilized zirconia is its low fracture toughness due to the cubic phase (C) ($\sim 1\ MPa\cdot\sqrt{m}$), which can lead to a rapid failure during thermal cycling [17,19].

However, a benefit that characterizes zirconia with a high yttria content is its low thermal conductivity, making it suitable for these applications. It was already experimented that increasing the yttria content in zirconia reduces thermal conductivity [20,21].

Electron Beam-Physical Vapour Deposition (EB-PVD) [22,23], Atmospheric Plasma Spraying (APS) [7], and Suspension Plasma Spraying (SPS) [24,25] techniques are commonly employed to apply the ceramic top coats of a TBC. However, EB-PVD is a costly process primarily utilized in aviation gas turbines. Atmospheric Plasma Spraying (APS) is the most used deposition method for the larger components of land-based gas turbines. By injecting powders into the plasma jet produced by a plasma gun, it is possible to produce either a porous or a dense vertically cracked (DVC) microstructure [26]. In this context, the characteristics of the feedstock powders play a crucial role in obtaining performant thermal barrier coatings [27]. The particle size of powders for the APS process is typically between 10 and 100 μm. Particles that are too large tend not to melt completely, while finer particles do not penetrate the plasma and tend to stay in the colder regions, resulting in inadequate heating in flight [28]. The morphology of the powders also affects their melting and flow behaviour during the APS process. Indeed, feedstock powders can be processed using different techniques to achieve the desired properties and functionality. The most common processes include fusing and crushing, agglomeration and sintering, and agglomeration and spheroidization (resulting in hollow spherical powders, HOSP). Fused and crushed powders are made by fusing mixtures of oxides in a furnace, followed by crushing [27]. The resulting particles are angular and blocky. Agglomeration and sintering is the most commonly used process, where agglomeration of fine primary particles is done by spray drying, and the aggregates are then consolidated by either liquid- or solid-state sintering [29,30]. HOSP involves a plasma fusion method to produce hollow microspheres, that is used instead of the sintering step on spray an drying particles. According to the literature, the advantage of using a HOSP morphology resides in a more uniform melting behaviour during the spray process [31].

Chi et al. studied the thermal conductivity of 8YSZ coatings with various microstructures obtained using different powders, such as agglomerated and sintered, fused and crushed, and HOSP powders [32]. Their findings demonstrated that using HOSP powders resulted in as-sprayed coatings with a higher content of interlamellar pores. The presence of interlamellar pores and splat interfaces in the coating significantly impacted thermal conductivity reduction even after thermal cycling test and isothermal exposure [33–35]. However, there is still little literature on the effect of the feedstock powder production route (hence, the powder particles' morphology) on other important TBC's properties, such as thermal cycling resistance and CMAS corrosion resistance. Moreover, little is known about how the feedstock powder morphology affects the characteristics of compositions different from "standard" 8YSZ, such as high-yttria compositions.

Therefore, this paper aims to evaluate the influence of Agglomerated and Sintered (A&S), Hollow Spherical (HOSP), and Fused and Crushed (F&C) ZrO_2–7-8 wt% Y_2O_3 (7-8YSZ) and ZrO_2–55 wt% Y_2O_3 (55YSZ) powders on the CMAS resistance of atmospherically plasma sprayed (APS) TBCs. All three powder types were employed to produce both porous and DVC 7-8YSZ monolayers to examine their resistance to CMAS infiltration, thermal cycling fatigue, and the top-coat/bond coat adhesion behaviour. Furthermore, the same tests were conducted on bi-layer systems consisting of a bottom porous layer of 7-8YSZ and a top porous layer of 55YSZ. After these tests, FEG- SEM, EDX, and micro-Raman analyses on the coatings were performed. High-speed nano-indentation and pillar-splitting methods were employed to measure hardness, elastic modulus, and fracture toughness across various material compositions [36]. High-speed nanoindentation is an innovative technique for characterizing materials at the nanoscale, providing a comprehensive set of data points, including hardness and indentation modulus. It finds valuable applications in mapping the mechanical properties of heterogeneous materials, making it particularly relevant for the characterization of TBC systems [37]. The pillar splitting method involves nanoindentation of micro-pillars created using a focused ion beam (FIB), enabling the straightforward calculation of fracture toughness based on the indentation load required to split the pillar, the pillar radius, and the hardness/modulus ratio of the material. This approach eliminates the need for crack length measurements and is unaffected by residual stresses, as they are released during the FIB milling process. Furthermore, the impact of FIB damage on fracture toughness measurement is minimized compared to other micro-scale methods, as crack initiation and growth occur primarily from the less affected core of the pillar [38].

2. Material and methods

2.1. Feedstock materials and coating deposition

Agglomerated and Sintered (A&S), Hollow Spherical (HOSP), and Fused and Crushed (F&C) 7-8YSZ and 55YSZ powders (Table 1) were used to produce six monolayers and 12 bi-layer coating systems deposited by APS technology (Table 2). DVC and porous microstructures were obtained using powders from the selected manufacturing routes but with different particle size distributions (PSD) to achieve the desired microstructure in terms of porosity and cracks density: a finer particle size for the DVC microstructure, a coarser particle size for a porous microstructure.

The thickness of the single-layer coating systems was designed to be

Table 1
list of feedstock materials.

Composition	Particle size distribution: d_{10} / d_{50} / d_{90} [μm]		Manufacturing process
	Fine	Coarse	
ZrO_2_7-8 wt% Y_2O_3	18/36/58	23/55/94	Agglomerated and sintered
	19/33/55	37/65/105	Fused and crushed
	16/35/59	21/53/86	HOSP
ZrO_2_55 wt.% Y_2O_3	19/40/72		Agglomerated and sintered
	20/35/58		Fused and crushed
	45/75/106		HOSP

Table 2
list of tested samples.

ID	Bottom layer	Bottom layer microstructure	Outer layer	Outer layer microstructure	TBCs architecture
AD	7-8YSZ	DVC	–	–	Monolayer
HD		DVC	–	–	
FD		DVC	–	–	
AP		porous	–	–	
HP		porous	–	–	
FP		porous	–	–	
AAP		porous	55YSZ	porous	Bi-layer
HHP		porous	55YSZ	porous	
FFP		porous	55YSZ	porous	

~1000 μm for the DVC and ~ 400 μm for the porous microstructure to ensure a comparable level of thermal conductivity. This choice was made to align with industry standards for turbine part coatings. The DVC layer is not commonly used for very low thickness coating as a porous TBC due to concerns related to crack formation and thermal conductivity [26,28,39]. Conversely, the porous structures generally are applied in a 400–600 μm thickness range on blades and vanes [40].

The bi-layer systems were produced using A&S, F&C, and HOSP powders with different architectures in terms of the relative thickness between the layers or of the total thickness (Fig. 1) to study the effect of thickness and thickness ratio on the properties of the coatings.

The top layer was deposited immediately after the bottom layer deposition. This sequential deposition process ensures a high surface temperature (>300 °C), when the deposition of the top layer starts. This promotes the adhesion between the layers. The ceramic coatings were applied using a Lincotek Equipment S.p.A cascade plasma torch in the APS R&D spray booth at Lincotek Rubbiano S.p.A. and proprietary process parameters optimized for porous and DVC microstructures, respectively.

All coatings were sprayed onto a Hastelloy-X substrate (coupons of 3 mm thickness and 25.4 diameter) with ~200 μm of a High-Velocity Oxygen-Fuel (HVOF)-APS "Flash" NiCoCrAlY bond coat (Höganäs Amperit 415®) followed by vacuum heat treatment at 1100 °C for 2 h. The final bond coat roughness was Ra > 10 μm (measured by a Mitutoyo SJ210 portable roughness tester with *cut-off* λ = 0.8).

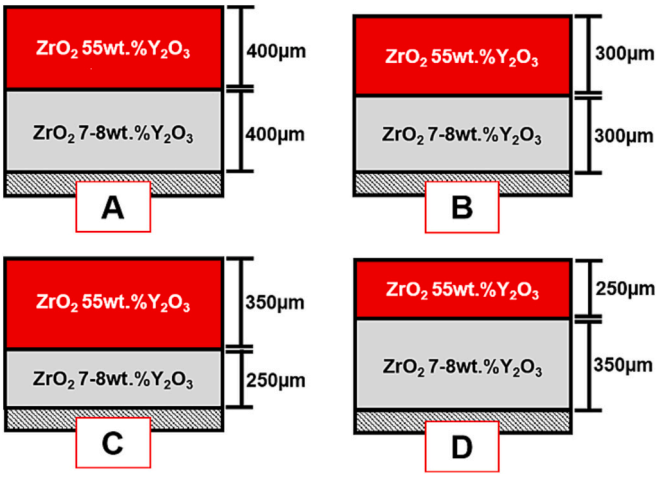

Fig. 1. Thickness distribution for bi-layer systems.

2.2. Nanoindentation high-speed mapping

To establish a foundational understanding of the load-indentation depth relationship for high-speed mapping and allow the selection of optimal indentation parameters, preliminary nanoindentation tests were performed under Continuous Stiffness Measurement (CSM) mode [41]. Indentations were carried out on bi-layer coatings, probing the properties of both the 7-8YSZ bottom and 55YSZ top layer. These experiments were executed using a G200 Nanoindenter from KLA Corporation, fitted with a Berkovich tip. The maximum penetration depth was 500 nm, and the indentations were carried out with a constant strain rate of 0.05 1/s. Calibration for the machine's frame stiffness and the tip area function was achieved through measurements on a certified fused quartz reference, adhering to the ISO 14577 standard. Notably, data indicating low modulus and hardness were excluded, as they were linked to cracks and porosity.

High-speed nanoindentation mapping was carried out over a wide area [37,42,43] of $100 \times 650\,\mu m$ on the coating cross-section. The mapping area includes the NiCoCrAlY bond coat, the 7-8YSZ bottom layer, and the 55YSZ top layer. A total of 7161 indents was performed for high-throughput mapping of the mechanical properties and identification of local heterogeneities in their distribution. The high-speed nanoindentation method, based on the same principles as the standard Oliver-Pharr one [41], benefits from specific improvements in the measurement hardware, electronics, and data management, allowing to realize an high number of tests in short times (from 1 to 5 s for a complete load-unload sequence). A two-dimensional map of hardness and elastic modulus represents the main output of a high-speed nanoindentation experiment. The maps were conducted in load-control mode to achieve precise repeatability of the indents, being the instrument a force-controlled one. The target load for testing was chosen based on the preliminary load-indentation depth relationships from CSM quasi-static nanoindentation, with the target of attaining an average indentation depth on the ceramic phases of ~ 300 nm. The spacing between the indents followed a 10-times-of-the target-depth rule, a new criterion recently introduced by Phani et al. [44], a set base that, for ceramics, can be stressed even to a 5-times setpoint.

In this case, the machine compliance and indenter area function were calibrated employing the same high-speed methodology (same dynamical testing conditions as the maps) with varied loads on a certified Fused Quartz reference sample before and after testing.

2.3. Fracture toughness measurement via pillar-splitting

The pillar-splitting technique, a brainchild of Sebastiani et al. [38,45], was employed to delve into the micro-scale fracture toughness of each layer within the bi-layer top coat. This innovative approach hinges on the precise nanoindentation of pillars, meticulously crafted via focused ion beam (FIB) micro-milling. The pillar-splitting technique offers an elegant approach to deducing fracture toughness. The method requires only the measurement of the pop-in indentation load, indicative of pillar failure. The dimensionless coefficient, γ, was obtained as a function of the hardness/modulus ratio by Finite Element Modelling (FEM). This coefficient's variation has been explored in prior research [46], considering different material properties and sharp indenter angles, including popular ones like Berkovich and Cube-Corner indenters. Two significant advantages of this method are: (a) there is no need to measure the crack length as cracks form spontaneously during indentation, and (b) the results are not influenced by residual stresses, which are typically released during the FIB milling process [38,45]. In this

Table 3
Chemical composition of the synthesized CMAS mixture (wt.%).

Oxide	CaO	MgO	Al_2O_3	SiO_2
Concentration (wt.%)	33	7	12	48

work, the γ coefficient's values were derived from the hardness and modulus values obtained by CSM nanoindentations corresponding to the FIB-milled pillars' positions. We crafted pillars having a diameter (D) of 4.5 μm and an aspect ratio $h/D \geq 1$ using a Helios Nanolab 600 FIB/SEM microscope (ThermoFisher Scientific) to an average number of 15 pillars per each constitutive phase of the top coat (given its heterogeneity) to strengthen the statistical reliability of the findings. A multi-step semi-automated FIB milling procedure with automated drift correction and alignment was used, involving a coarse milling phase that employs a current of 0.92 nA at 30 kV and a final multi-step polishing and edge sharpening phase at 93 pA and 30 kV.

Some pillars were FIB-sectioned after fabrication to accurately measure the actual diameter and taper angle and investigate the presence of pre-existing cracks in the sample material.

Pillar splitting tests utilized a Keysight G200 nanoindenter with a Berkovich tip calibrated to ISO 14577 standards on Fused Quartz. Using a strain rate of 0.05 1/s, tests continued until the pillar's unstable failure, marked by a pop-in on the load-displacement curve. Fracture toughness for each yttria layer was derived from at least six split pillars.

2.4. Tensile adhesion/cohesion test

The adhesion test was performed by preparing the samples following ASTM C633. FM1000 polyamide-epoxy adhesive discs, cured in a muffle furnace for 90 min at 170 °C, were used to glue the samples to the mating caps. The assembled samples (three for each architecture) were tested at a 1 mm/min standardized loading rate using an electromechanical test system (MTS Criterion Model 43).

Specifically, bi-layer samples' tensile adhesion/cohesion tests were carried out only on the system with the architecture shown in Fig. 1A. In fact, the ASTM C633 standard dictates that a layer must be at least 380 μm thick to ensure consistency in the test results, preventing the glue from penetrating through the porosity down to the substrate interface.

The failed samples were observed with an optical microscope (LEICA DMI3000M) to identify the failure location.

2.5. CMAS corrosion testing

The CMAS suspension was prepared by mixing the oxides according to the percentages given in Table 3 [22]. MgO, $CaCO_3$ and SiO_2 (< 325 mesh, Sigma-Aldrich) and Al_2O_3 (Martoxid MR-70, Martinswerk, Bergheim, Germany) were blended with water in 1:2 proportion in weight and deposited on half of the surface of the coupons with a 0.2 g/cm^2 area density of slurry, equivalent to 0.064 g/cm^2 area density of solid phase. A heat treatment was performed on all the samples in a muffle furnace in air for 1 h at 1250 °C [17].

The test was performed on all monolayer and bi-layer samples with the architecture shown in Fig. 1A. The goal of this test is primarily to verify the chemical interactions between the coatings and the CMAS melt; therefore, the specific architecture of the system is of lesser relevance in this case.

2.6. Thermal cycling test

The thermal cycling fatigue (TCF) resistance was evaluated using an automatic furnace. The TCF cycle consisted of rapid heating to 1100 °C (150 °C/min), an isothermal soaking at 1100 °C for 50 min, followed by a rapid cooling from 1100 °C to 100 °C with forced air (100 °C/min). The test was stopped when ~20 % of the surface area of the ceramic top coat was spalled (assessed by visual inspection) or after reaching a limit number of cycles. The results were expressed as the average ± standard deviation and were normalized with respect to a reference value. The test was carried out on all samples, including all bi-layer architectures shown in Fig. 1A–D to determine how the overall thickness and thickness ratio affect the TCF resistance. Three thermal cycling test

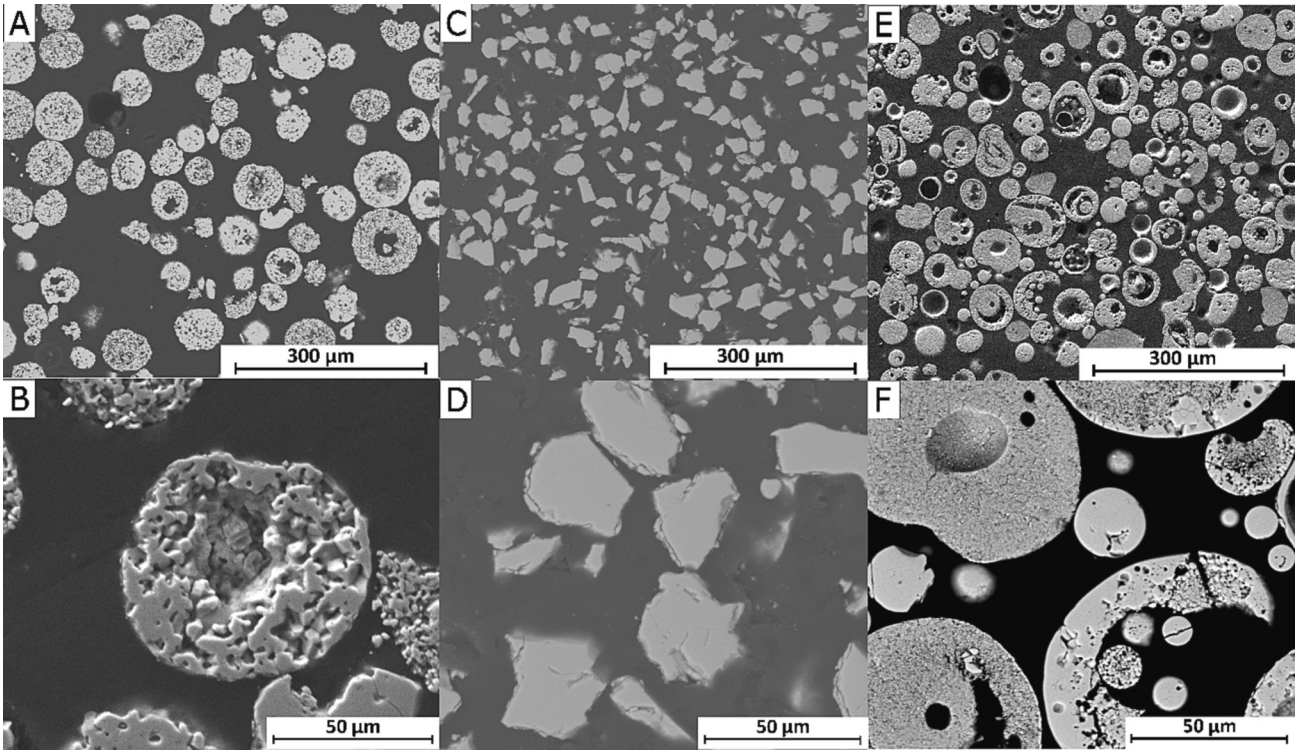

Fig. 2. BSE-SEM cross-sectional micrographs of the tested fine powders: A, B) agglomerated and sintered; C, D) fused and crushed; E, F) Hollow spherical powders.

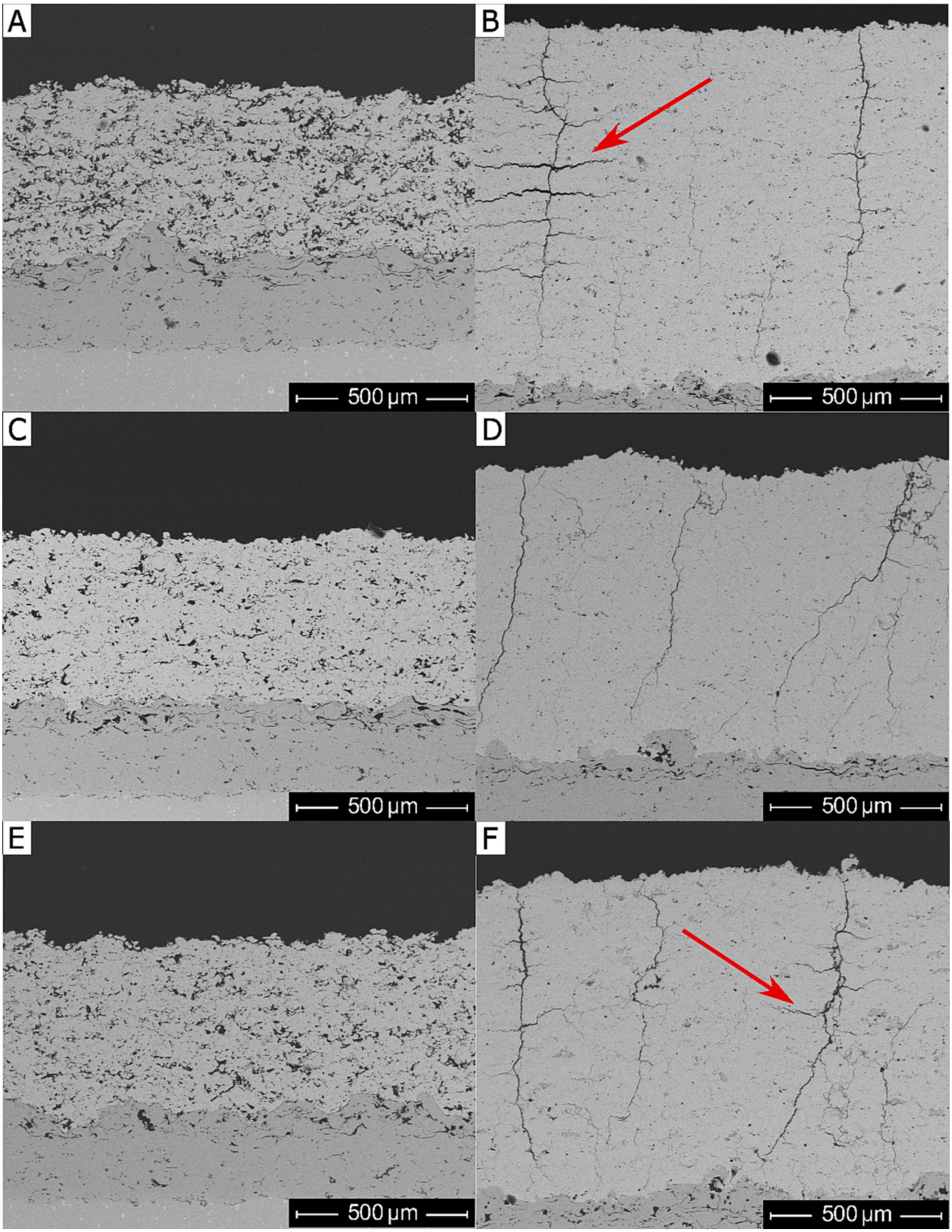

Fig. 3. SEM cross sectional micrographs of as sprayed coatings obtained by (A, B) agglomerated and sintered, (C, D) fused and crushed, and (E,F) HOSP powders: A, C, E – porous microstructures; B, D, F – DVC microstructures.

Table 4
Porosity values for all monolayer coatings.

Sample	Porosity [%]
AP	17.1 ± 1.5
FP	13.2 ± 1.2
HP	13.4 ± 1.1
AD	1.5 ± 0.2
FD	1 ± 0.1
HD	4 ± 0.3

repetitions were performed on as-sprayed top surfaces for each sample.

2.7. Samples' characterization

A structural and microstructural characterization was performed on "as-sprayed" samples, after thermal cycle fatigue testing and after CMAS corrosion. In each condition, the samples were cold-mounted in epoxy resin and cut with a resin-bound Al_2O_3 abrasive disc in a metallographic cutting machine (Micromet 20, Remet SAS, Casalecchio di Reno (BO), Italy). The resulting cross-sections were subsequently ground using SiC papers and polished with polycrystalline diamond suspension and oxide-polishing suspension for microstructural analysis. Cold-mounting, grinding and polishing were also employed to analyze the cross-sections of the feedstock powders.

Scanning electron microscope (SEM) micrographs, energy-dispersive X-ray (EDX) spectra and elemental maps were acquired using a Quanta-200 SEM system (FEI – ThermoFisher Scientific, Eindhoven, NL) equipped with an INCA (Oxford Instruments Analytical, Oxford, UK) EDX detector, operating with a 25 keV electron beam energy. The samples were sputter-coated with an Au layer to ensure electrical conductivity. In addition, detailed SEM micrographs were acquired using a Nova NanoSEM 450 (FEI – ThermoFisher Scientific) equipped with a field emission gun (FEG) source and a Quantax-200 (Bruker Nano GmbH, Berlin, Germany) EDX system equipped with an Xflash-6 detector. Some detailed micrographs were acquired at low electron beam energy (3 keV) on samples without the sputtered Au layer.

Porosity was measured using image analysis software (ImageJ – NIH, Bethesda, Maryland, USA) on optical micrographs at 100× magnification. Porosity was evaluated as the average of four measurements on micrographs randomly acquired on the coating cross-section. The same software was used to quantify the amount of CMAS that penetrated the 55YSZ top layer of the bi-layer coatings from high contrast BSE micrographs at 3000× magnification. The greyscale images were converted into "binary", black and white, to measure the percentage of CMAS-infiltrated areas. A greyscale threshold range was manually set to distinguish the CMAS-infiltrated region, having intermediate greyscale contrast levels, from the unaltered coating material, having brighter contrast, and the defects, i.e., empty pores, and cracks, coating, having darker contrast. Pixels with intensity values falling out of the greyscale threshold range were turned white, whilst those within the range were turned black, and their overall area fraction was then quantified. A total of five images were acquired and analysed for each sample.

Micro-Raman spectroscopy was performed using a LabRam (Horiba Jobin-Yvon, Longjumeau, France) spectrometer equipped with a "red" He:Ne laser (λ = 632.81 nm) and a "green" solid-state laser (λ = 532 nm), both focused through a 100× objective.

3. Results and discussion

3.1. Monolayer coatings

3.1.1. Powders' and coatings' microstructure

SEM micrographs were acquired on the three types of 7-8YSZ powders listed in Table 1 (Fig. 2). Hollow spherical powders have a large globular pore with a relatively thin outer solid shell, and they are much more porous than agglomerated, sintered, fused, and crushed powders (compare Fig. 2E to Fig. 2A). In particular, the fine porosity of the agglomerated and sintered powders probably makes it more difficult to

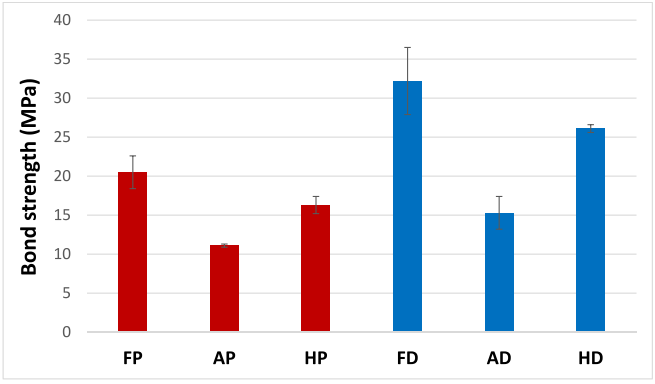

Fig. 5. Values of bond strength [MPa] of the monolayer coatings.

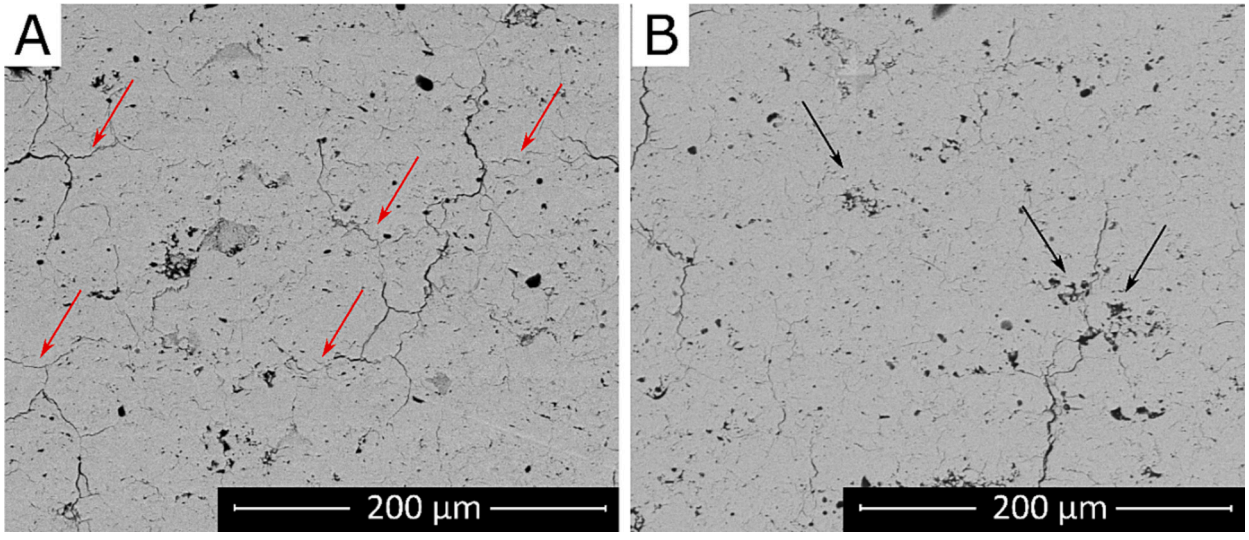

Fig. 4. Comparison between HD and AD microstructures at high magnification: A) intersplat boundaries (red arrows) in sample HD; B) intra-lamellae porosity in sample AD.

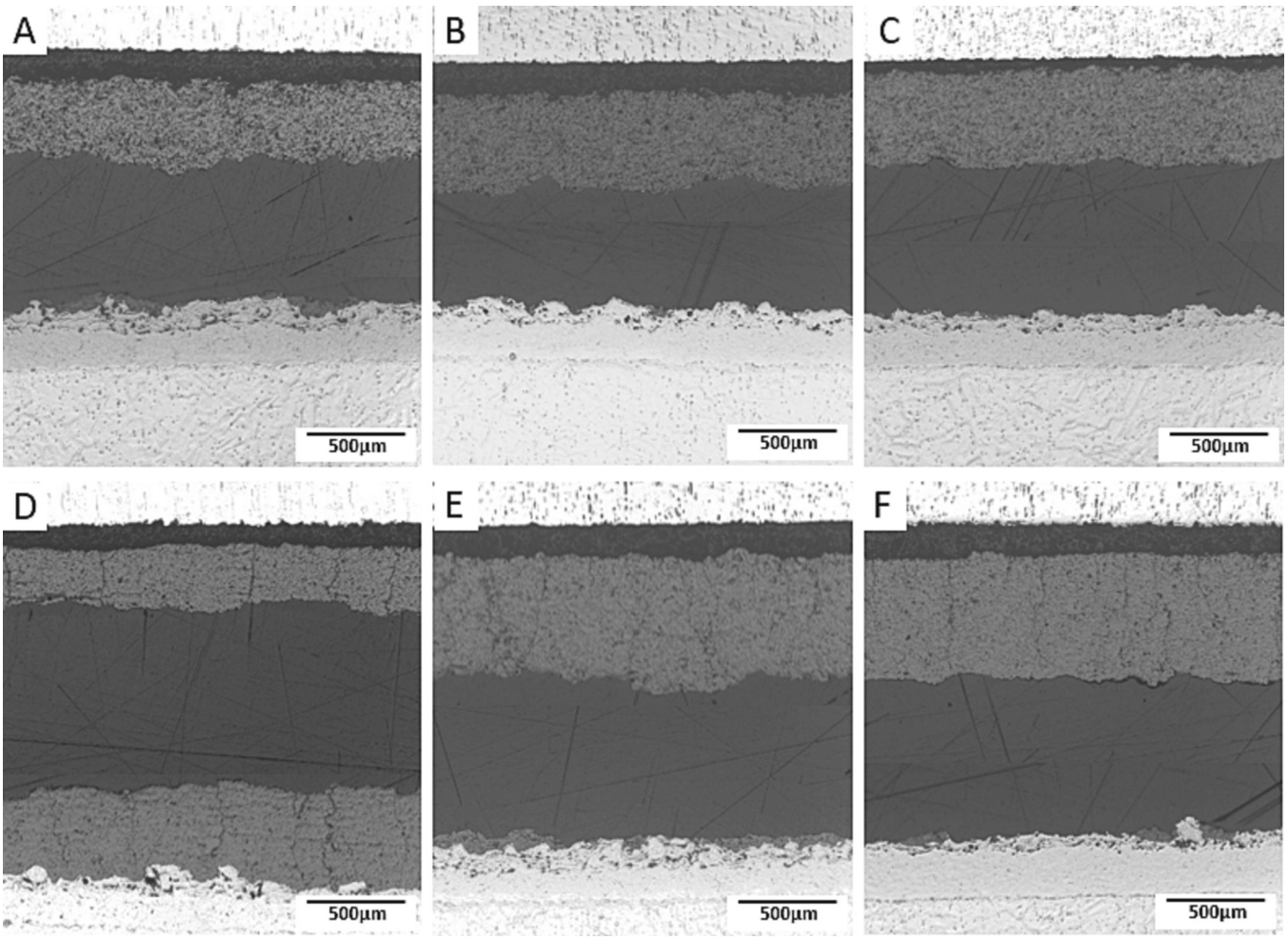

Fig. 6. Optical micrographs of 7-8YSZ monolayer coatings after adhesion tests: A) AP (porous coating, agglomerated and sintered feedstock); B) HP (porous coating, HOSP feedstock); C) FP (porous coating; fused and crushed feedstock); D) AD (DVC coating, agglomerated and sintered feedstock); E) HD (DVC coating, HOSP feedstock); F) FD (DVC coating; fused and crushed feedstock).

melt them completely during spraying, due to the low thermal conductivity. By contrast, the peculiar microstructure of the HOSP powders means that they likely melt more easily than the agglomerated and sintered ones with comparable particle size distribution. The complete melting of HOSP particles corresponds to a large deformation when they impact on the substrate. The fused and crushed powders exhibit a blocky-angular shape and have a higher density than the other powders (Fig. 2C,D). These characteristics usually make them more suitable for applications requiring low porosity, such as DVC coatings.

Coatings obtained with the three 7-8YSZ powders (A&S, HOSP and F&C) were designed with two different types of microstructures: dense-vertically cracked (DVC) TBCs and porous TBCs.

SEM overviews of the as-sprayed coatings are reported in Fig. 3. Table 4 shows the porosity values of all samples measured by image analysis.

Coatings obtained with the fused and crushed powders are denser and more compact than the others, both with a "porous" microstructure (Fig. 3C) and a DVC one (Fig. 3D). SEM micrographs revealed a noticeable distinction in DVC microstructures. Specifically, unlike the FD (Fig. 3D) sample, the AD (Fig. 3B) and HD (Fig. 3F) samples exhibited longitudinal branching of the transverse cracks along the deposition pass interface (Fig. 3 – red arrows). In the case of the agglomerated and sintered powders, this phenomenon may be attributed to the internal porosity, which can reduce the thermal conductivity at the individual particle level, making complete melting of the powders more challenging. With the HOSP powder, where this phenomenon is comparatively less marked (Fig. 3F), the reason could instead lie in the many splat interfaces. The volume of an individual lamella obtained by a HOSP particle is comparatively smaller than with the other powder types, once the flattening process eliminates the central cavity taking up much of the particle volume. Indeed, the final coating microstructure produced by the HOSP powders seems to be characterized by very thin lamellae. This is suggested by an SEM micrograph acquired at high magnification (Fig. 4A). It shows much more intersplat boundaries (Fig. 4A-red arrows), which is generally the reason for the lower thermal conductivity of coatings obtained with HOSP powders as reported in the literature [27], which is especially apparent in the DVC coating. It is even possible that some interfaces are relics of the inner cavity of the HOSP particles, if the flattening process did not cause a complete melding of the inner surfaces.

Conversely, A&S powders produce a coating with mostly intra-lamellar porosity (Fig. 4B – black arrows). The retention of many pores in partially unmelted particles can explain why the AP coating is the most porous (17 %). The process used for the deposition of a DVC layer promotes more extensive melting of the particle; thus, the porosity of the DVC coating obtained by the F&C powder is lower than that of the corresponding DVC coating obtained from the HOSP powder because, on the one hand, the blocky particles could be fully melted and, on the other, the greater solid volume (i.e. greater volume of the splat) and the lack of the central cavity resulted in fewer intersplat interfaces.

These considerations about the coatings' porosity are fundamental to understand the differences between the CMAS and TCF behaviour of the

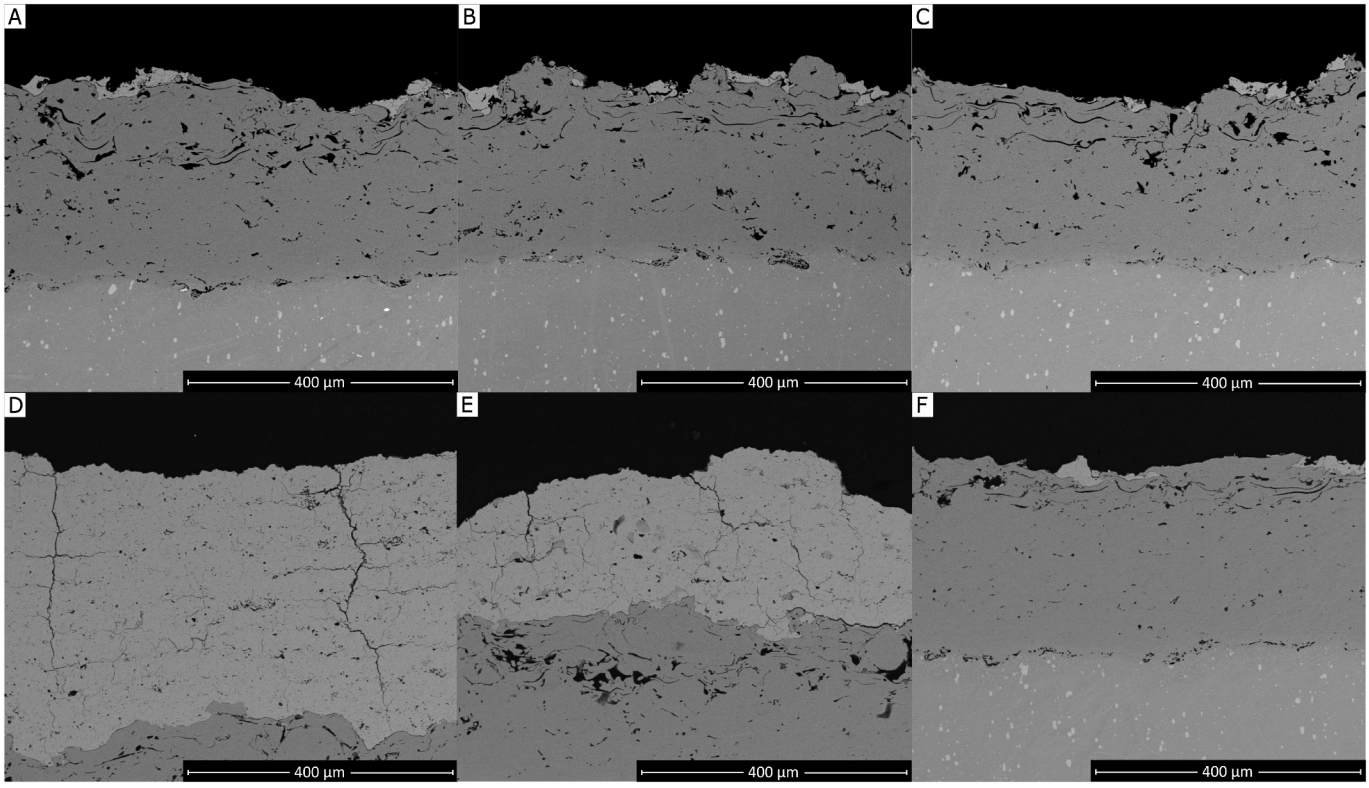

Fig. 7. SEM micrographs acquired at the interface between the bondcoat and 7-8YSZ top layer of monolayer coatings after adhesion tests: A) AP (porous coating, agglomerated and sintered feedstock); B) HP (porous coating, HOSP feedstock); C) FP (porous coating; fused and crushed feedstock); D) AD (DVC coating, agglomerated and sintered feedstock); E) HD (DVC coating, HOSP feedstock); F) FD (DVC coating; fused and crushed feedstock).

different microstructures in the subsequent sections.

3.1.2. Adhesion/cohesion test results

The results of the adhesion/cohesion tests indicate that the bonding strength is influenced by both the microstructure of the coating and the morphology of the powder used. Specifically, the porous and the DVC monolayer coatings demonstrated similar trends in adhesion strength as a function of the powder manufacturing route (Fig. 5). Still, every DVC coating showed ~1.5 times stronger adhesion to the substrate than the corresponding porous coating. For a given microstructure (either porous or DVC), the samples obtained from the agglomerated and sintered powders always resulted in the lowest adhesion strength, whilst the fused and crushed powder always resulted in the highest bond strength, so that the peak value of ~32 MPa was obtained by the FD sample, which also possessed the lowest porosity (Table 4).

From the optical micrographs (Fig. 6) and SEM micrographs (Fig. 7) acquired on failed samples after adhesion testing, it was observed that the failure in the FD sample (Figs. 6F and 7F) occurred mainly at the interface between the bondcoat and the top coat, indicating adhesive failure. This can be attributed to the high density, i.e. high cohesive strength of the coating. In contrast, AD (Figs. 6D and 7D) and HD (Figs. 6E and 7E) samples exhibited cohesive failure (intralayer rupture) and mixed failure, respectively. Specifically, the more magnified SEM view of Fig. 7E shows an area of mainly cohesive failure in sample HD; however, on the left-hand side of the micrograph, a crack running along the top coat/bond coat interface can also be seen. The lower-magnification view in the optical micrograph of Fig. 6E accordingly shows that, while some areas on the failed samples do have visible top coat residuals on the bond coat, others (e.g. in the centre of the micrograph) have little or no residuals, indicating mixed adhesive/cohesive failure. These results highlight the influence of the structural density on the adhesion test outcomes. The many, partially visible (i.e., not wholly tight) intersplat boundaries attributed to the peculiar microstructure of the HOSP powders, as discussed previously [34], are visible in the SEM image of Fig. 4A and, together with the longitudinal branching cracks, likely impaired the cohesive strength of the HD sample, with a measured tensile strength value of ~26 MPa compared to ~32 MPa in the FD sample. Similarly, the intra-lamellar porosity and branching cracks previously noted in the AD sample (Fig. 4B) explain the reduction in the cohesion strength of the AD sample (~15 MPa).

The FP coating also revealed the highest adhesion strength among the porous coatings (~20 MPa), followed by the HP (~16 MPa) and AP (~11 MPa) ones. In this case, SEM micrographs showed adhesive failure for all systems (Fig. 7A–C). Compared to the DVC ones, the increased porosity of these coatings results in a reduced contact surface area between the bondcoat and the topcoat, consequently impacting the adhesion resistance [47]. By contrast, the tighter interlamellar contact and the more continuous interface (with much fewer voids) in a DVC microstructure means they possess stronger adhesion and cohesion than the porous samples.

3.1.3. CMAS corrosion resistance

CMAS attack caused severe failure of all porous TBCs due to infiltration of the silicate melt into the microstructure, regardless of the powder used. The penetration of molten CMAS into the porous coatings is extensive, occurring through open pores and grain boundaries. This results in a significant separation between the splats and the unmolten or re-solidified particles (Fig. 8). Because the microstructure obtained by fused and crushed powders was denser than the others, the FP coating retained better cohesion between the splats even after CMAS corrosion than the AP and HP samples. Specifically, the separation between the splats and the formation of globular/filament structures along the inner pore surfaces are more evident in the AP and HP samples (Fig. 8B,F). At the same time, in the FP one this mechanism is confined to the outer surface (Fig. 8D – red arrows). The Raman spectra obtained from the cross-sectional views of the porous coatings (Fig. 9) show distinct peaks

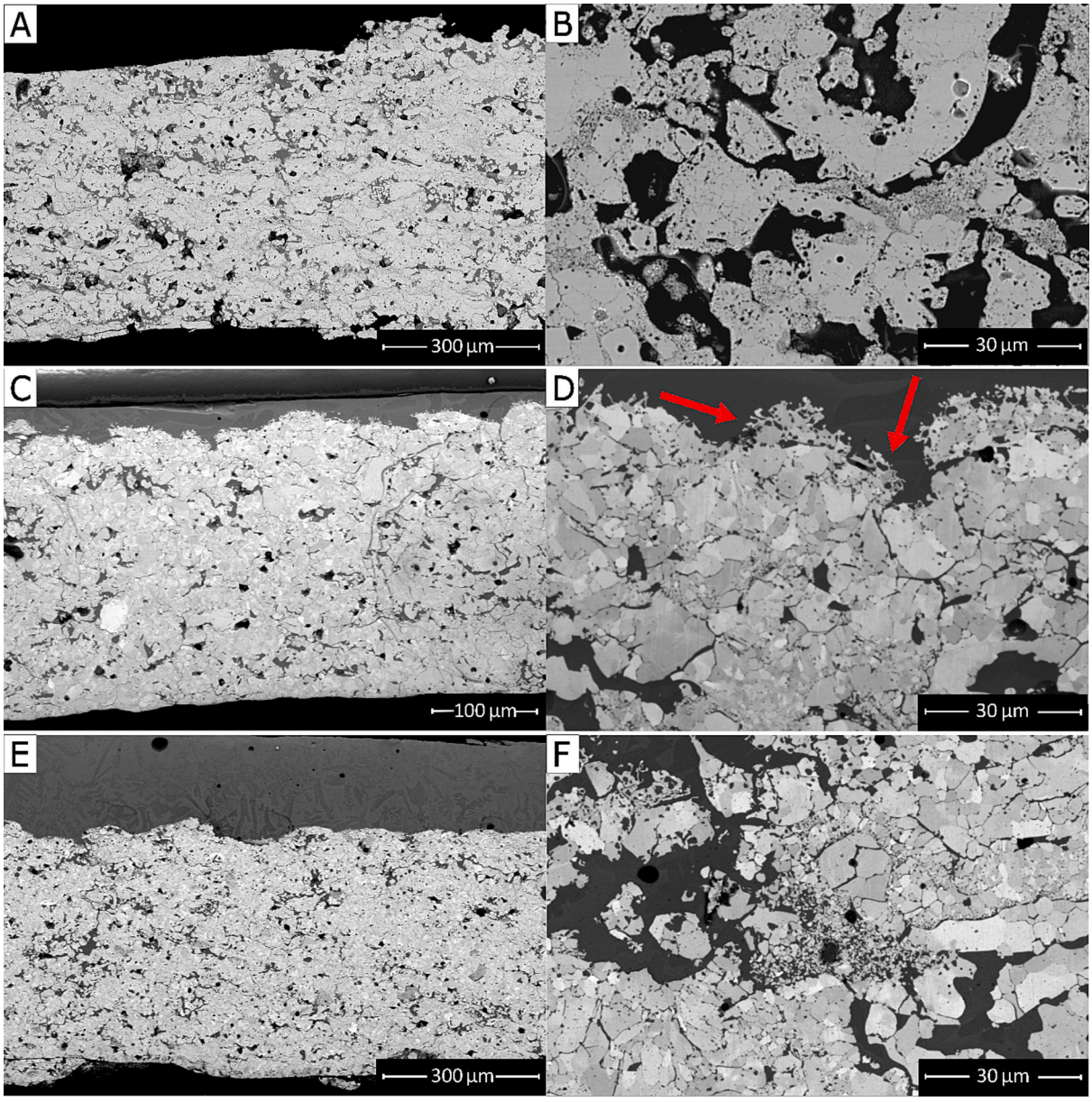

Fig. 8. SEM cross sectional micrographs of (A, B) AP (agglomerated and sintered, 7-8YSZ), (C, D) FP (fused and crushed, 7-8YSZ), (E, F) HP (HOSP, 7-8YSZ) samples after CMAS attack.

that can be attributed to the tetragonal zirconia phase, which were identified in the denser areas of all samples (Fig. 9 – spectra 2, 4, and 6).

Conversely, weaker peaks of monoclinic zirconia were observed in the proximity of the porosities and on the outer surface of all samples (Fig. 9 – spectra 1 and 3). As CMAS interacts with YSZ, it dissolves the material along its grain boundaries and progresses toward the interior. This interaction can cause the complete detachment of YSZ grains from each other. Subsequently, yttria-depleted zirconia precipitates from a saturated melt, forming distinct globular or fibrous structures composed of the transformable (t) phase at elevated temperatures. Upon cooling to room temperature, these structures undergo a martensitic transformation, converting to the monoclinic (m) phase [22,48–50].

The effect of CMAS corrosion was mitigated on the DVC systems, although those coatings were also wholly delaminated from the bond coat (Fig. 10). It can be noticed that the degree of corrosion changed with the morphology of the corresponding feedstock powders.

Generally, in DVC samples, CMAS infiltration mainly occurred along the transverse and branching cracks (where present). This is confirmed by EDX elemental maps acquired on sample HD (Fig. 11). In this regard, the infiltration of the CMAS melt was characterized by quantitative EDX analysis of the chemical composition in two different areas of each coating: 1) on the outer layer and 2) on the inner layer, as shown in Fig. 10. In the AD and FD samples, CMAS-related oxides were detected in greater amounts in areas adjacent to the surface (Table 5 – spectrum 1), while much fewer CMAS-related oxides were found in the inner layer of the coating (Table 5 – spectrum 3). The FD sample exhibits enhanced corrosion resistance attributable to its lowest porosity and the absence of the branching phenomenon. By contrast, a higher amount of CMAS-related oxides was revealed in the inner layer of sample HD (Table 5 – spectrum 3), meaning that the intersplat boundaries allow the CMAS melt to penetrate more efficiently, even along the dense parts of the coating.

Thus, it can be concluded that using fused and crushed powders can positively impact the coatings' CMAS resistance, regardless of their microstructure. This is attributed to the higher coating density achieved when using these powders compared to other options.

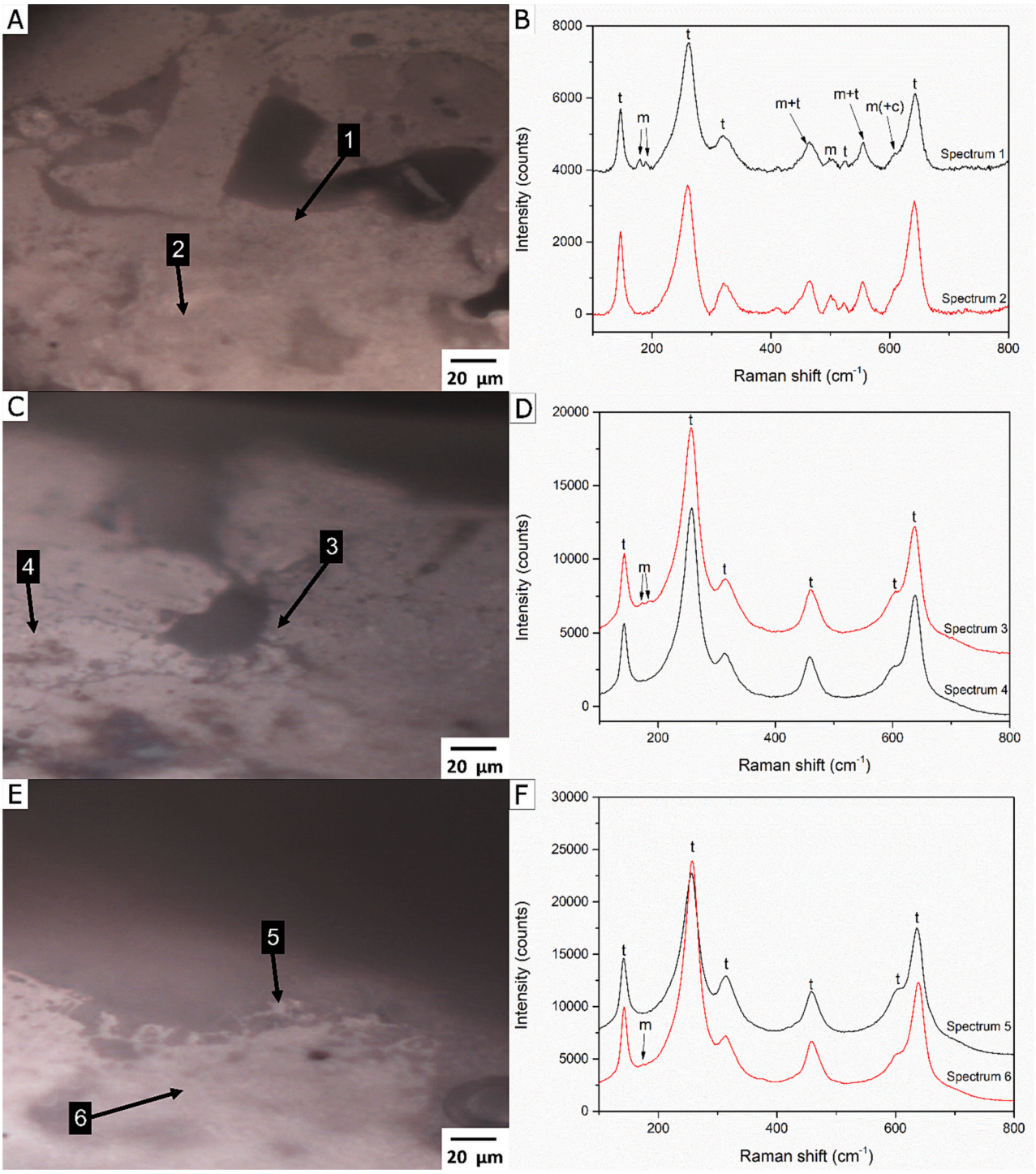

Fig. 9. Optical micrographs of the AP, FP and HP coatings after CMAS corrosion (A, C, E), and corresponding micro-Raman spectra (B, D, F). Labels m and t indicate peaks assigned to monoclinic and tetragonal zirconia crystalline phase.

As noted above, according to Fig. 10, the delamination of all DVC TBCs occurs at the interface between TGO and the coatings. This observation indicates that the primary cause of failure of CMAS-infiltrated DVC TBCs is the cold shock, i.e. as the CMAS solidified within the transverse cracks during cooling, it stiffened the coating and compromised its strain tolerance. The resulting stress build-up thus led to delamination [51].

3.1.4. *Thermal cycling resistance*

The results of thermal cycling fatigue testing performed on all samples are reported in Fig. 12. All porous systems have excellent resistance to thermal cycling and were removed from the furnace at the same number of cycles (well above an OEM acceptance level) in perfect conditions. Thus, it was impossible to establish whether the micro-structural differences among porous coatings are relevant to their overall thermal cycling fatigue resistance. Still, in any case, the micro-structure is irrelevant to attaining a functionally satisfactory performance.

The SEM micrographs of all three porous systems after the TCF test, presented in Fig. 13, reveal that the average thickness of the TGO is

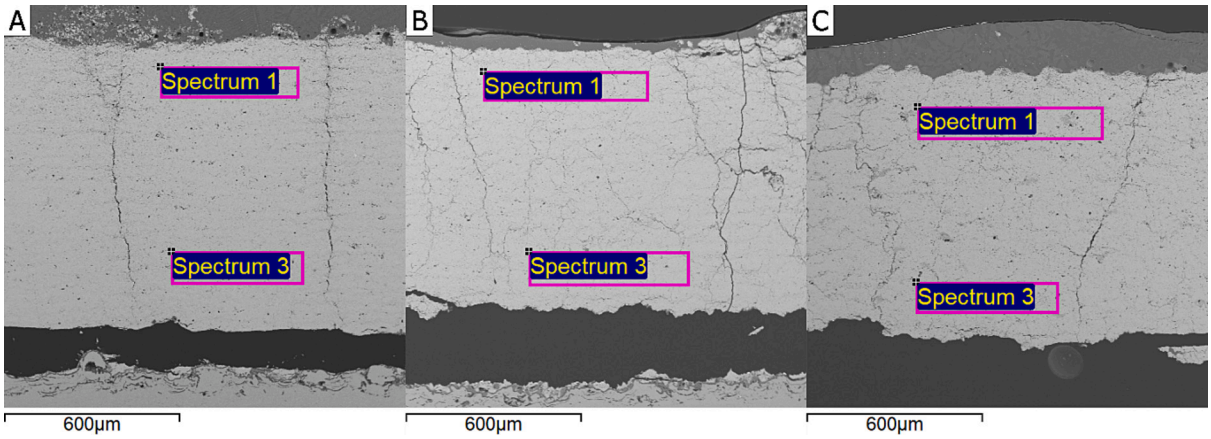

Fig. 10. EDX analysed areas: spectrum 1 acquired on the outer layer; spectrum 3 acquired on the inner layer of A) AD (agglomerated and sintered, 7-8YSZ); B) FD (fused and crushed, 7-8YSZ); C) HD (HOSP, 7-8YSZ) after CMAS corrosion test.

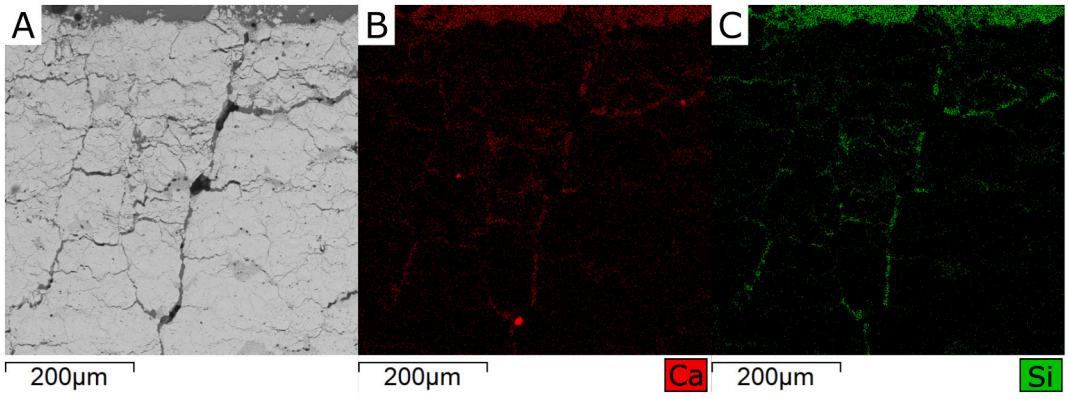

Fig. 11. EDX maps acquired on the cross section of sample HD after CMAS corrosion.

Table 5
Quantitative analysis of the oxides [%] present in samples A) AD; B) FD; C); HD. Spectrum 1 was acquired on the outer layer; spectrum 3 was acquired on the inner layer. The table is referred to Fig. 10.

Sample	Acquisition area	MgO [%]	Al_2O_3 [%]	SiO_2 [%]	CaO [%]	Y_2O_3 [%]	ZrO_2 [%]	HfO_2 [%]
AD	Spectrum 1 (Fig. 10 A)	0.52	0.32	1.52	1.28	3.50	91.75	1.11
	Spectrum 3 (Fig. 10 A)	–	–	1.29	0.98	5.94	89.80	2.00
FD	Spectrum 1 (Fig. 10 B)	0.31	0.35	1.29	1.43	4.48	90.35	1.79
	Spectrum 3 (Fig. 10 B)	–	–	0.60	0.98	5.80	92.63	1.54
HD	Spectrum 1 (Fig. 10 C)	0.06	0.78	2.11	1.86	3.86	89.55	1.78
	Spectrum 3 (Fig. 10 C)	–	0.55	2.00	1.45	4.96	88.91	2.13

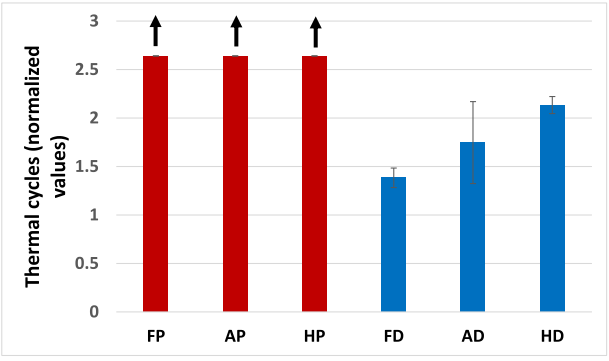

Fig. 12. Normalized number of thermal cycles to failure for the monolayer coating.

approximately 5 µm. This value falls within the critical thickness range [52], which, if exceeded, would result in coating failure. The micrographs also reveal the occasional formation of mixed oxide protrusions, recognizable by their intermediate greyscale contrast level (in between that of the alumina-based TGO and the YSZ layer), as well as internal oxidation of the APS "Flash" bond coat layer.

Furthermore, the SEM micrographs also reveal that some cracks did propagate along the top coat, close to the interface between the TGO. This type of cracking is typical of plasma-sprayed porous TBCs, and it has been documented frequently in the literature. It is driven by the complex stress state near the top coat/TGO interface because of the mismatch in thermal expansion coefficient and the rough profile of the bond coat surface [53–55]. However, the lack of complete delamination of the coating is due to the porosity of the microstructure, which contributes to the relaxation of stresses.

Therefore, it is reasonable to assume that despite being removed

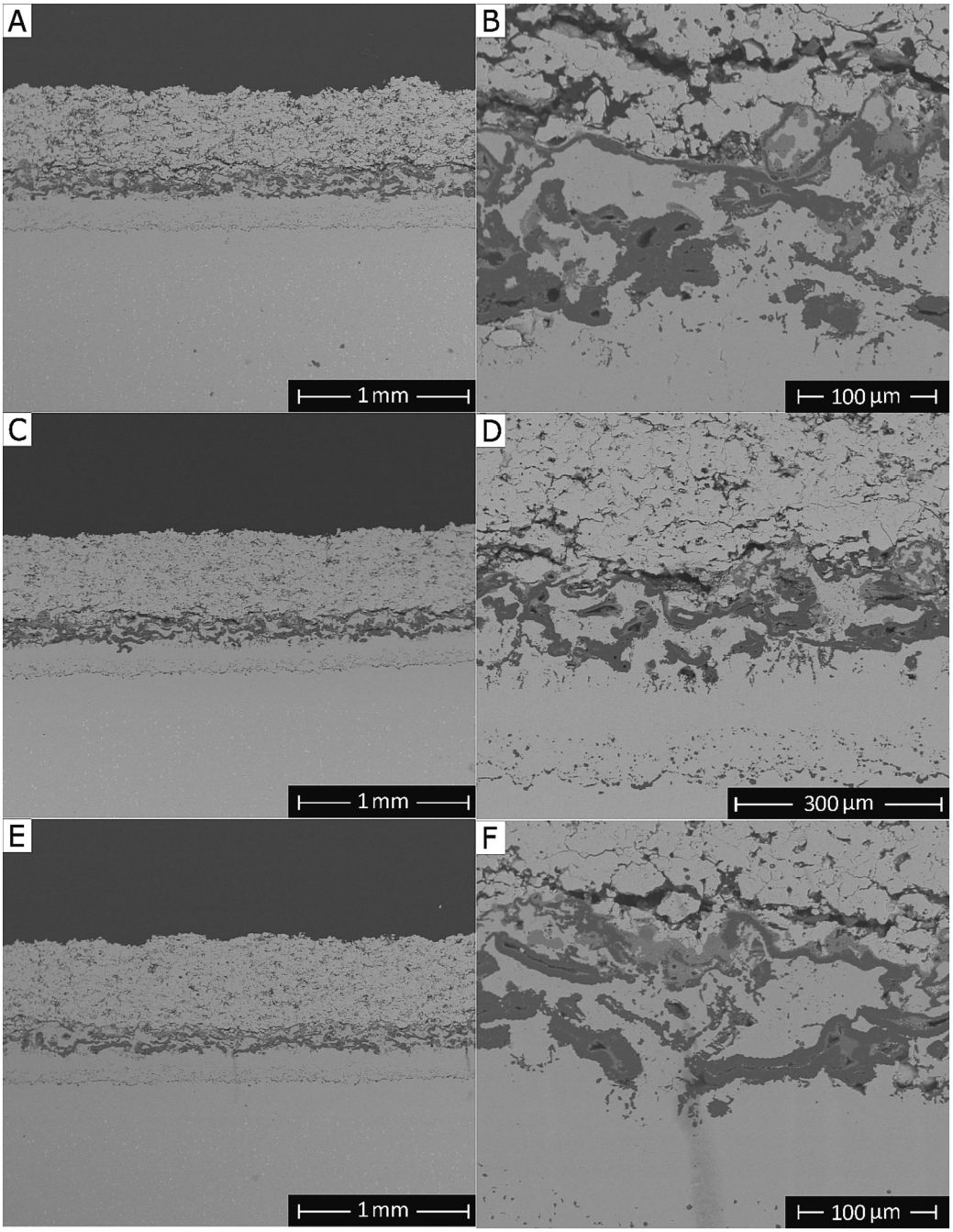

Fig. 13. SEM micrographs of A) AP (agglomerated and sintered, 7-8YSZ); C) FP (fused and crushed, 7-8YSZ); E) HP (HOSP, 7-8YSZ) and corresponding micrographs acquired the TGO layer: B) AP; D) FP; F) HP after thermal cycling test.

from the furnace while still in good working condition, all the porous samples tested were nearing the end of their useful life. This is because the growth margin of the TGO is very narrow.

On the other hand, the thermal cycling behaviour of the various DVC samples shows significant differences (Fig. 12). The results contrast entirely with the CMAS response: the DVC coating produced from the HOSP powders achieved more extended TCF durability. At the end of the TCF test (2.1 normalized cycles), the surviving portion of the HD top coat still appears attached to the bondcoat (Fig. 14E,F). However, it should be noted that prolonged exposure to high temperatures can result in the depletion of aluminium in the bondcoat, which in turn can lead to coating spallation. When the aluminium content is depleted, oxides such as chromia can form (Fig. 15). TGO growth accompanied by oxidation of heavier elements such as chromium can be the cause of the failure of the coating. Although the HD sample exhibits a layer of heavy oxides, it appears more compliant than other DVC samples. This can be attributed to many, not fully bonded intersplat boundaries within the coating. These boundaries reduce the stiffness of the coating, offering additional pathways for stress relief and allowing the coating to withstand external forces and deformation better.

To the contrary the worst TCF response is given by the FD sample (Fig. 12), probably due to its higher density, which makes the coating stiffer and prone to develop more significant thermal stresses. Both AD and FD samples failed due to cracks propagating across the top coat, going from one roughness crest of the bond coat to the next.

Notably, it appears that the microstructure of the DVC system, hence its compliance, is much more influential on the TCF response than the tensile adhesion/cohesion strength, as testified by the fact that the FD

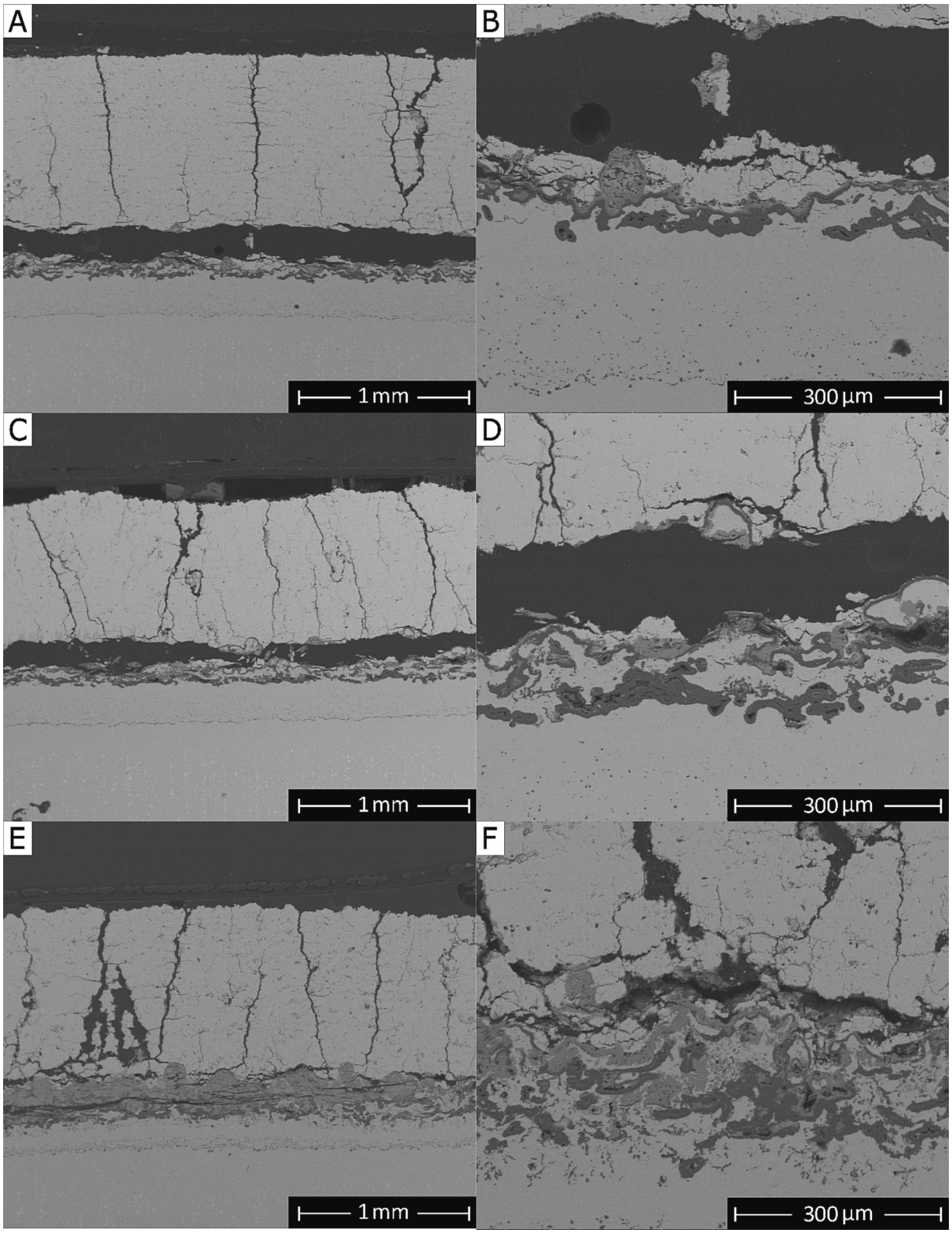

Fig. 14. SEM micrographs of A) AD (agglomerated and sintered, 7-8YSZ); C) FD (fused and crushed, 7-8YSZ); E) HD (HOSP, 7-8YSZ) and corresponding micrographs acquired on the TGO layer: B) AD; D) FD; F) HD after thermal cycling testing.

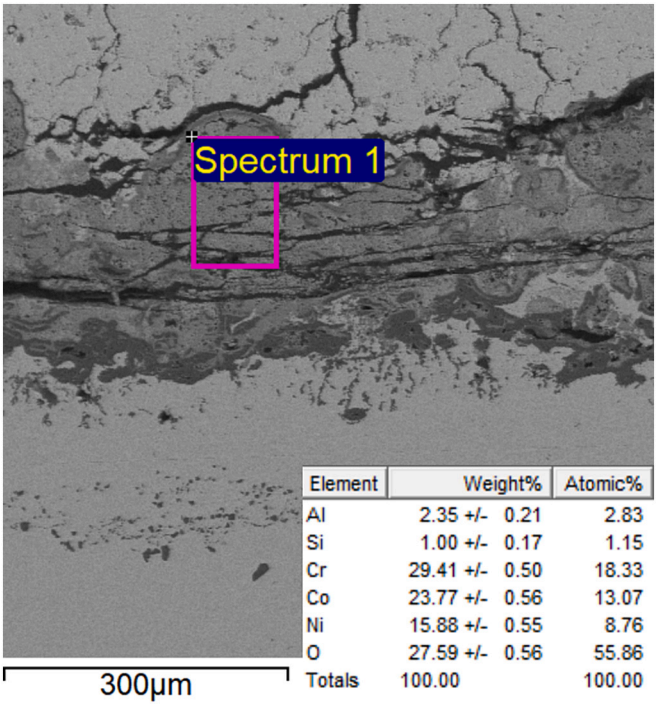

Element	Weight%	Atomic%
Al	2.35 +/- 0.21	2.83
Si	1.00 +/- 0.17	1.15
Cr	29.41 +/- 0.50	18.33
Co	23.77 +/- 0.56	13.07
Ni	15.88 +/- 0.55	8.76
O	27.59 +/- 0.56	55.86
Totals	100.00	100.00

Fig. 15. EDX and relative semi quantitative analysis of HD acquired at the interface between the substrate and the top layer.

sample exhibits the earliest TCF failure despite having the highest tensile strength. Indeed, the TCF failure mode is much different than that induced in a tensile test set-up.

3.2. Bi-layer coatings

3.2.1. Powders' and coatings' microstructure

Based on the state of the art, multi-layer TBCs were designed to overcome the disadvantages of 7-8YSZ in contact with CMAS as seen above. Furthermore, as recalled in the Introduction, the deposition of multilayer systems enhances the thermal stability of the coatings, particularly at temperatures exceeding 1200 °C. For this purpose, bi-layer systems consisting of a 55YSZ outer layer and a 7-8YSZ as bottom coating were produced (Fig. 16D-F). Three different powder morphologies were employed for the deposition of 55YSZ top coat (Fig. 16A-C).

In all bi-layer systems, the porosity of the 55YSZ layer is consistently lower than that of the 7-8YSZ layer. The porosity values of the as-sprayed bi-layer (architecture A) coatings are listed in Table 6. These results represent all architectures with different thickness ratios, as mentioned previously in Fig. 1.

This difference is mainly due to the particle size used for depositing the 55YSZ layer (Table 1). Smaller particles have a greater ease of melting, leading to a more compact coating. The selection of smaller particles was a deliberate choice to produce a denser outer layer that effectively prevents CMAS oxide penetration. In contrast, coarser particles (Table 1) were chosen for depositing the 7-8YSZ layer. The greater porosity of the 7-8YSZ layer enables it to withstand the stresses and strains that arise during operation, as witnessed by the excellent results in the TCF tests of the porous monolayer systems while still providing sufficient thermal insulation.

3.2.2. Assessment of layers' mechanical properties

The Continuous Stiffness Measurement (CSM) grid was instrumental in determining the hardness and elastic modulus variations attributed to the different yttria content in the YSZ ceramic layers. From the CSM

Table 6
Porosity values of the bi-layer systems with architecture A.

Sample	Porosity [%]	
	7-8YSZ	55YSZ
AAP-A	15.5 ± 1.1	7.7 ± 0.4
FFP-A	12.4 ± 1.3	6.5 ± 0.7
HHP-A	12.5 ± 1.0	7.1 ± 0.5

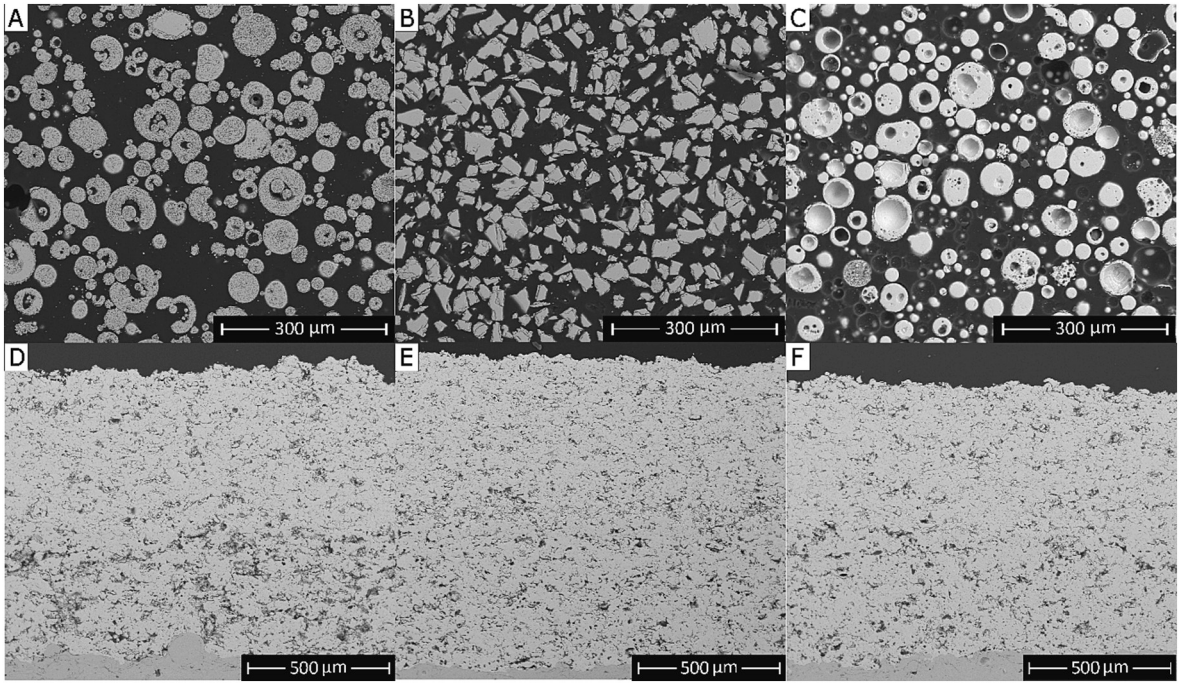

Fig. 16. BSE-SEM cross-sectional micrographs of 55YSZ powders: A) agglomerated and sintered; B) fused and crushed; C) Hollow spherical powders and respective micrographs of as sprayed bi-layer coatings: A) AAP-A; B) FFP-A; C) HHP-A.

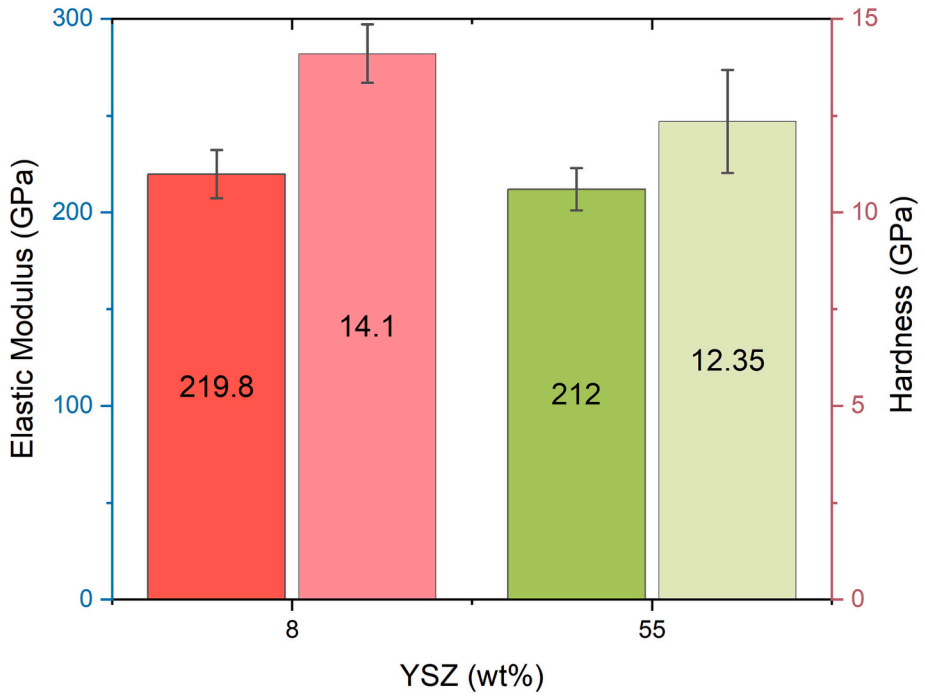

Fig. 17. Elastic modulus and indentation hardness values obtained by nanoindentation in Continuous Stiffness Measurements mode, averaged across valid tests performed on homogeneous and defect-free splats in the layers with different wt% yttria concentration.

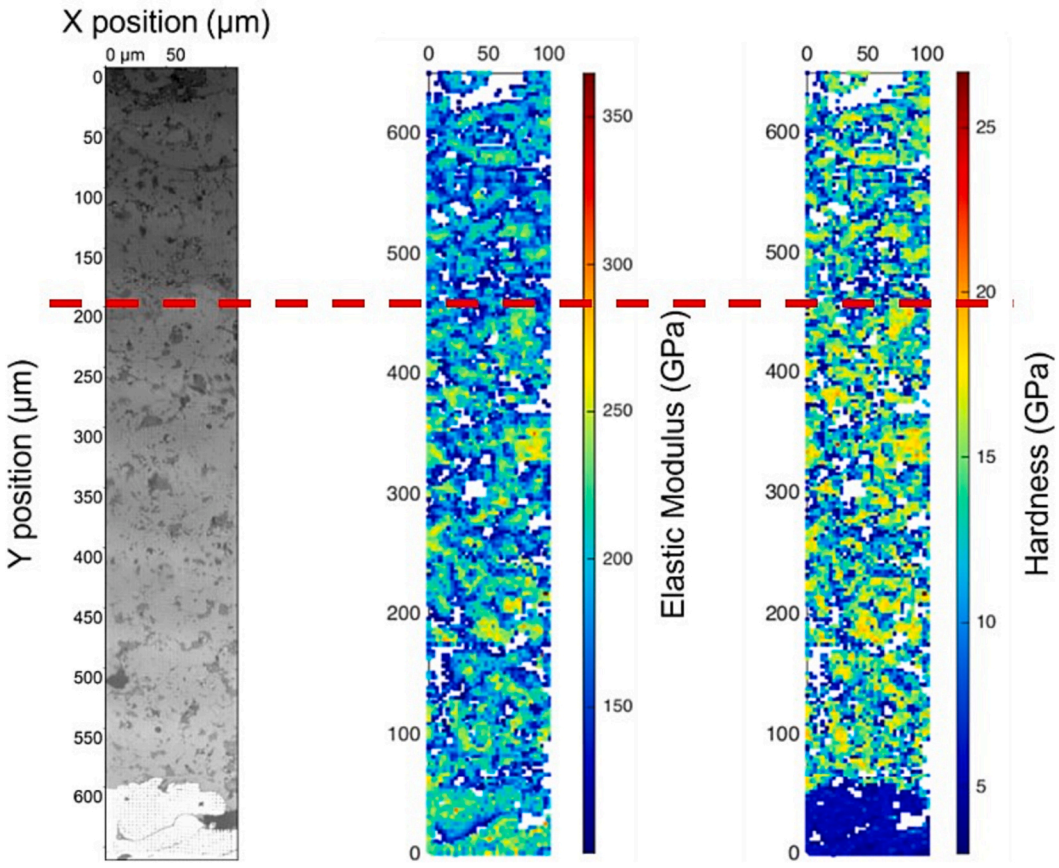

Fig. 18. Optical view of the area indented of FFD sample at high speed (100×, Leica DCM3D profilometer), accompanied by the refined maps of elastic modulus and hardness covering the entire TBC coating cross-section. This spans from the bond coat (depicted in bright and dark blue in the optical and hardness maps, respectively) through the 8 wt% yttria bottom layer and up to the 55 wt% yttria top coat.

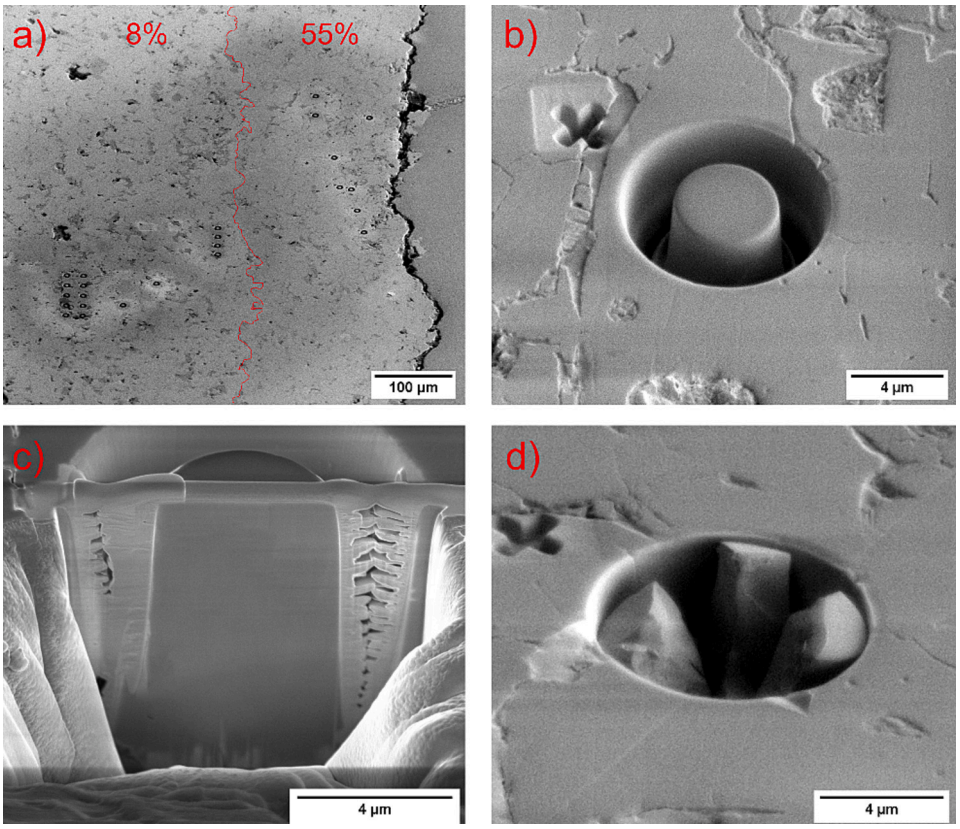

Fig. 19. Micro-pillar splitting process includes: a-b) creating 4.5 µm diameter pillars for each TBC coating layer to ensure consistency; c) using FIB to examine pillar shape and taper angle; and d) a post-test image showcasing a representative fracturing process after indentation.

Table 7
Critical loads (P_c), calibration coefficients, and fracture toughness values as calculated from pillar splitting experiments as a function of the wt% of yttria.

Wt.% yttria	P_c (mN)	γ (CSM)	K_c ($MPa\sqrt{m}$)
7–8	15.46 ± 0.52	0.314	2.22 ± 0.39
55	23.9 ± 4.2	0.339	1.43 ± 0.17

measurements, the average values for elastic modulus and hardness were 219.8 GPa and 14.1 GPa for the 8YSZ and 212 GPa and 12.35 GPa for the 55YSZ (Fig. 17). These results align with findings from the literature, where the yttria content influences the mechanical properties of YSZ coatings [37,56]. It is important to remark that, due to the small size of the indents, these values reflect the "intrinsic" properties of the ceramic material at the intralamellar level, rather than the "overall" properties of the coating, being insensitive to microstructural features like interlamellar boundaries, pores, cracks, etc.

A decline in the elastic modulus and hardness of 55YSZ compared to 7-8YSZ was observed, emphasizing the critical role of yttria content in determining the mechanical attributes of these materials.

High-speed nanoindentation mapping was conducted over the cross-section of the entire coating, as shown in Fig. 18, revealing the mechanical properties and heterogeneities across the bond coat, 7-8YSZ bottom layer, and 55YSZ top layer. In particular, the maps corroborate the slightly higher harness and modulus of the 7-8YSZ material composing the underlying layer, compared to the 55YSZ composition of the top layer. Lower hardness and elastic moduli are systematically found next to pores and defects because, as an indentation mark approaches the defect, the affected volume of material around the indent encompasses the defect region, resulting in reduced load-bearing ability and, therefore, lower measured values of elastic modulus and hardness. Although this feature can be considered a measurement artefact, it also underlines the critical importance of pores in compliance with the structure, thus corroborating the previous discussions on the TCF response.

The pillar-splitting method provided insights into the micro-scale fracture toughness of each layer in the top coat. A scheme of the fabrication of pillars is reported in Fig. 19.

The fracture toughness of the 7-8YSZ material was 2.22 ± 0.388 MPa$\sqrt{m}$, while a lower value of 1.43 ± 0.169 MPa$\sqrt{m}$ was observed for the 55YSZ material (calculations are summarized in Table 7). Fig. 20 showcases the reliability of the pillar-splitting method. The distinct trends in the observed pop-in events during the tests were indicative of the unstable failure of the pillars and combined with the gamma coefficient for splitting as evaluated from CSM measurements, further confirming the derived fracture toughness values.

The lower toughness of the 55YSZ composition is consistent with the literature. As the yttria content grows above approximately 15 wt%, the cubic phase© is retained to room temperature, though at first only in a thermodynamically metastable form [57]. This phase is known to possess lower fracture toughness (~1 MPa·$\sqrt{m}$) [58] compared with the non-transformable "phase composing the 8YSZ layer because it does not possess its ferroelastic toughening mechanism, nor the transformation-toughening mechanisms typical of partially-stabilized zirconia polycrystals based on slightly lower yttria concentrations (e.g. 6 wt%Y_2O_3 – ZrO_2). Notably, the fracture toughness values measured in this work are consistent with those Mercer et al. reported [58] for t'-ZrO_2 stabilized with 7 wt% Y_2O_3 (~3 MPa•$\sqrt{m}$) and for cubic ZrO_2 with 20 wt% Y_2O_3 (~1.1 MPa•$\sqrt{m}$). Especially for the present 7-8YSZ layer, the slightly lower value measured in this work compared with the data from Mercer et al. might be explained by its rather high porosity as noted in the previous section. Namely, it is possible that some pores or lamellar interfaces were present within the volume of some of the pillars, although

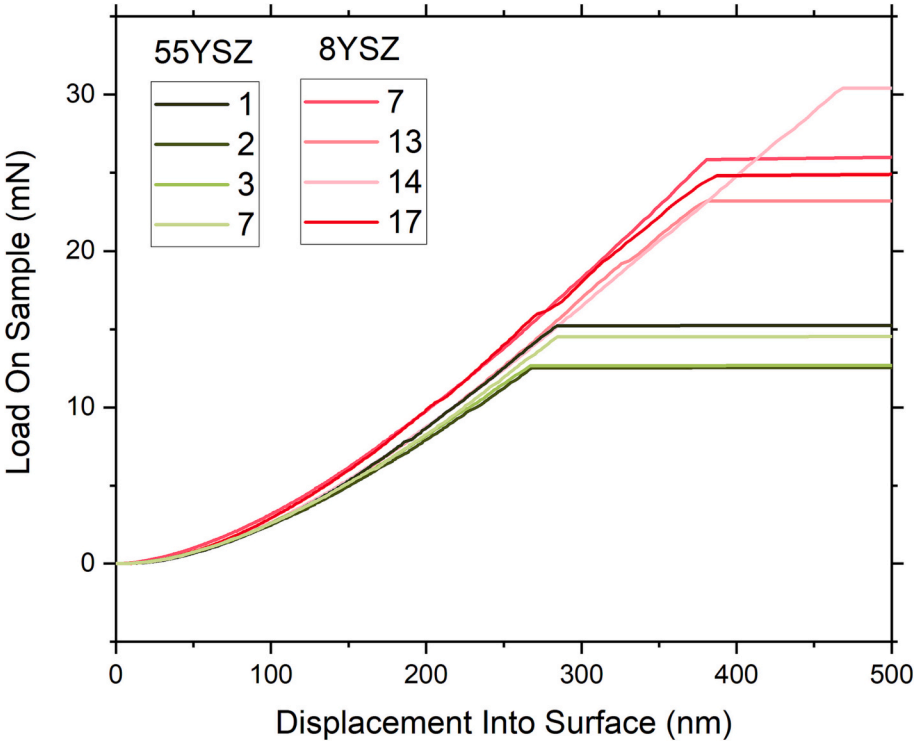

Fig. 20. Load On Sample versus Displacement Into Surface curves corresponding to representative micro-pillar splitting experiments performed on the 7-8YSZ and 55YSZ layers.

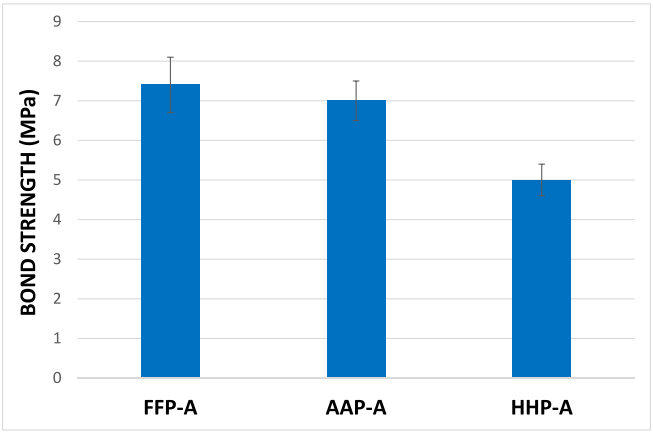

Fig. 21. Values of tensile adhesion/cohesion strength [MPa] of the bi-layer coatings, measured on samples with individual layer thickness of 400 μm.

none was seen in the example of Fig. 19c. Their presence would reduce the critical load for splitting and, therefore, the measured toughness, in comparison to the "intrinsic" fracture toughness of the material. This effect might have been less relevant for the 55YSZ top layer due to its higher density, hence a lower likelihood of defects within a pillar.

3.2.3. *Adhesion/cohesion test results*

As explained in the "Material and methods" section, tensile adhesion/cohesion tests were carried out on the systems shown in Fig. 1A, i.e. the AAP-A, FFP-A, and HHP-A systems, which exhibited greater layer thickness than other architectural designs. ASTM C633 requires a minimum layer thickness of 380 μm to prevent the glue from penetrating through the porosity down to the substrate interface. The higher strength value was obtained by the FFP-A (7.4 MPa) sample followed by AAP-A (7.0 MPa) and HHP-A (5 MPa) (Fig. 21). As for the porous single-layer systems, the fused and crushed powders ensure greater strength than the other powder manufacturing routes.

Furthermore, the bi-layer systems exhibited lower tensile strength values when compared to single-layer architectures. This behaviour could be attributed to the reduced mechanical interlocking between the two layers, caused by the lower roughness of the bottom layer (7-8YSZ) in contrast to that of the bondcoat. Indeed, the post-test analysis by optical imaging (Fig. 22A-C) as well as by SEM inspection (Fig. 22D-F) reveals that in all the bi-layer systems, regardless the powder manufacturing route, the failure occurred at the interface between the 7-8YSZ and 55YSZ layers. No intra-layer failure was detected, and no or almost no residuals of the 55YSZ layer were found onto the 7-8YSZ one (Fig. 22D-F). The failure between the two layers is considered favorable because the outer layer (55YSZ) could be sacrificed. In contrast, the bottom layer (7-8YSZ) remains intact and continues to fulfill the thermal barrier coating function.

3.2.4. *CMAS corrosion resistance*

After the CMAS attack, it was observed that a few microns of the 55YSZ top coat in all bi-layer systems (architecture-A) had spalled off (Fig. 23).

The interaction between CMAS and the coatings brought about significant alterations in the microstructure of the outer surface of 55YSZ. Most notably, it led to the transformation of large grains within the coating into more spherical or globular structures surrounded by a phase with an intermediate greyscale contrast level between the coating and the CMAS phase (Fig. 24A-C). Upon closer examination, EDX spectra of these intermediate grey areas (see the areas marked as "spectrum 1" to "spectrum 3" in Fig. 24A-C) reveal intense peaks of silicon and yttrium (Fig. 24D). This suggests a new phase precipitated due to the interaction between the CMAS and the coatings. Micro-Raman spectra acquired in these areas corroborate the existence of a yttrium-enriched silicate, as indicated by the peak at 875 cm^{-1}, along with a weak, broad band suggesting the presence of cubic zirconia crystalline phase (Fig. 24E). Hence, it can be concluded that a yttrium-based silicate emerges as the

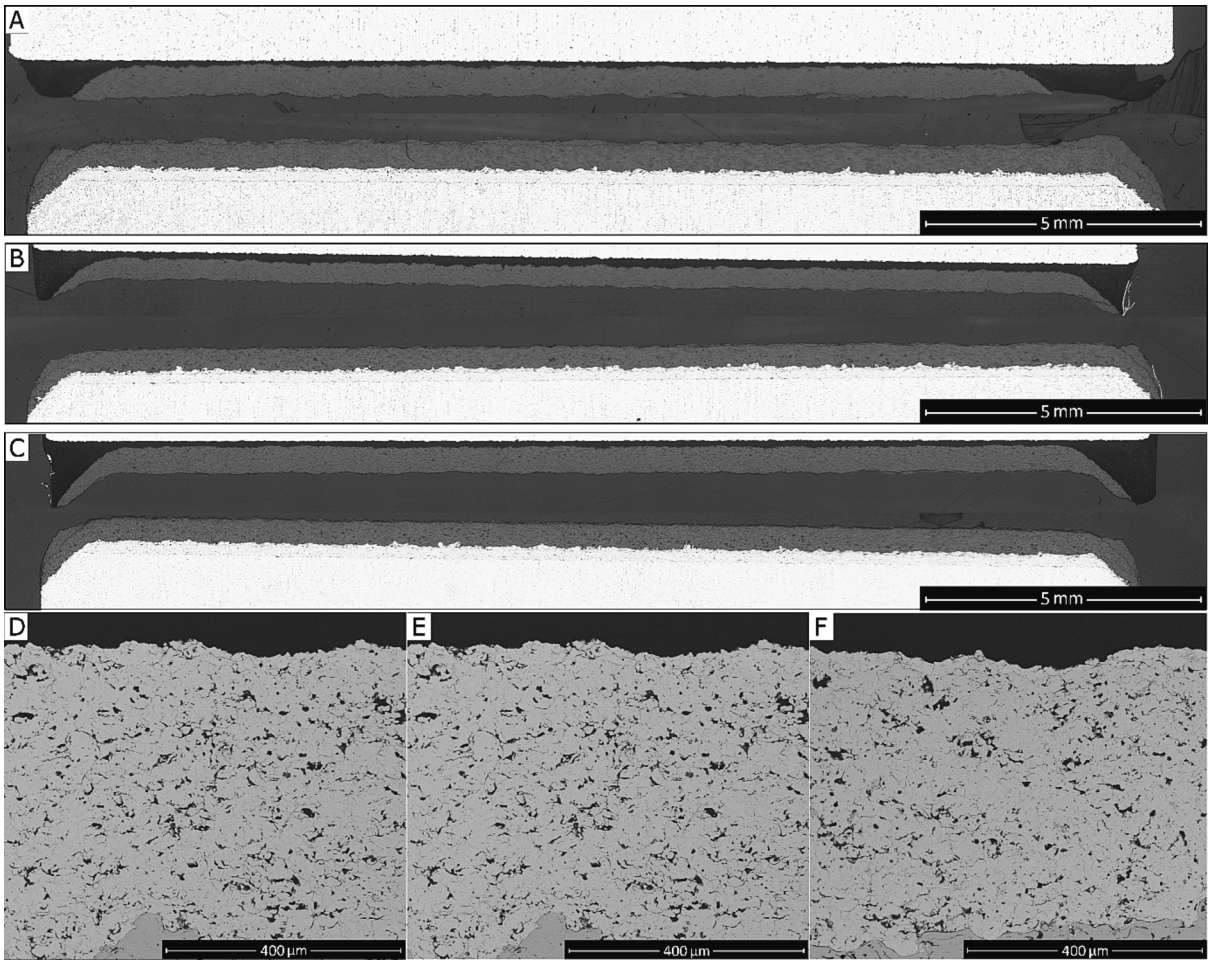

Fig. 22. Optical overviews of bi-layer systems: A) AAP-A (agglomerated and sintered feedstock); B) FFP-A (fused and crushed feedstock); C) HHP-A (HOSP feedstock) after adhesion testing, and high magnificated SEM micrographs of the same samples: D) AAP-A; E) FFP-A; F) HHP-A.

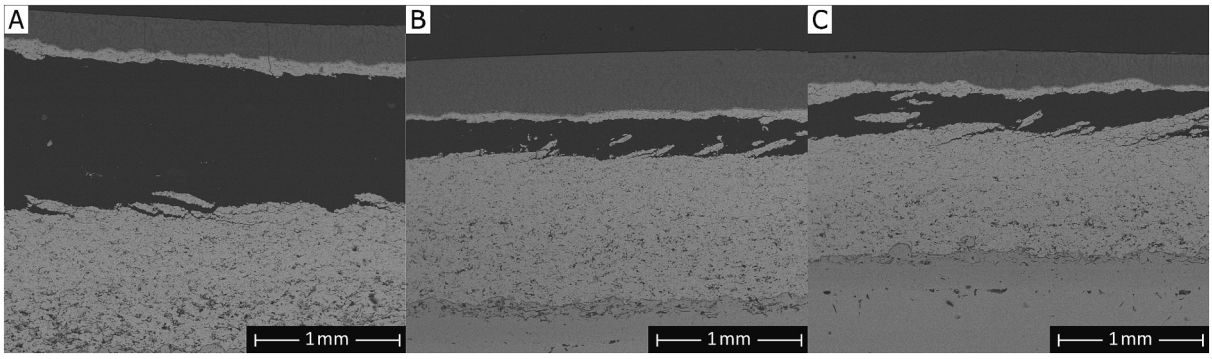

Fig. 23. BSE SEM micrographs of A) AAP-A (agglomerated and sintered feedstock); B) FFP-A (fused and crushed feedstock); C) HHP-A (HOSP feedstock) after CMAS attack.

primary reaction product when CMAS interacts with ZrO_2–55 wt% Y_2O_3.

Previous researches [17,59,60] have pointed out that the respective optical basicity values strongly influence the reaction between CMAS and the coating. The optical basicity (Λ) of a compound or a mixture of binary oxides, the latter being calculated as $\Lambda = \sum_i X_i \Lambda_i$, where X_i and Λ_i are respectively the mole fraction of the *i*-th constituent of the mixture and its optical basicity [59], is a crucial factor in determining its reactivity with other oxide compounds or mixtures. Specifically, compounds with a greater difference in optical basicity to CMAS tend to react more strongly with the latter. They are more likely to form new compounds that can develop into protective layers, blocking further interactions. On the other hand, compounds with an optical basicity close to that of CMAS are likely to dissolve easily without any reaction product.

The calculated optical basicity of 55YSZ is 0.99 [17], which is significantly different from that of CMAS (0.69) [59]. This explains the formation of a yttrium-rich silicate during the CMAS corrosion test.

Interestingly, most of the residual coating layer that remained attached to the bond coat seemed undamaged and did not exhibit any significant changes in its microstructure (Fig. 25A-C). Further analysis

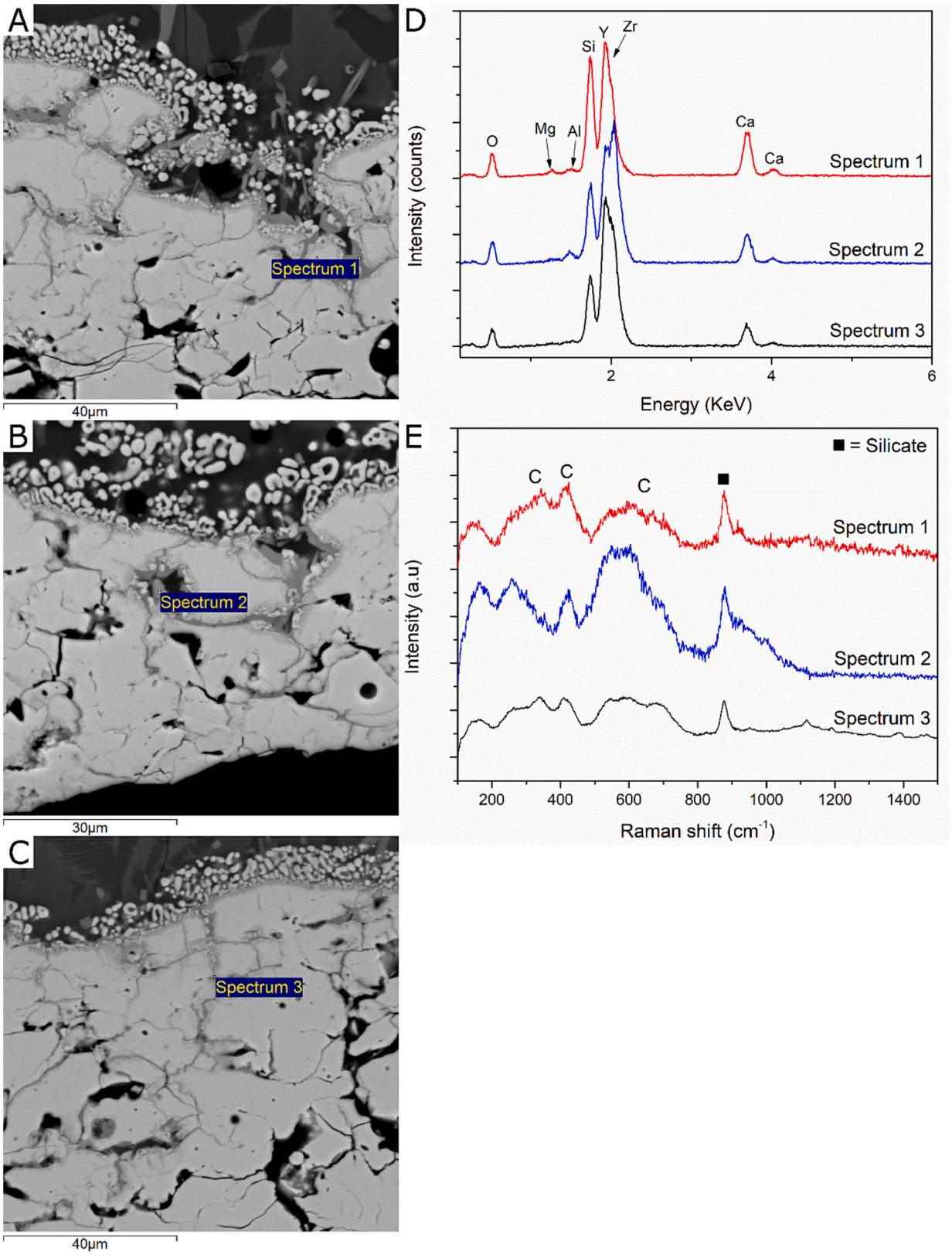

Fig. 24. SEM micrographs acquired at high magnification on the 55YSZ portion detached after CMAS attack: A) AAP-A (agglomerated and sintered feedstock); B) FFP-A (fused and crushed feedstock); C) HHP-A (HOSP feedstock); corresponding EDX analyses (D) and micro-Raman spectra (E).

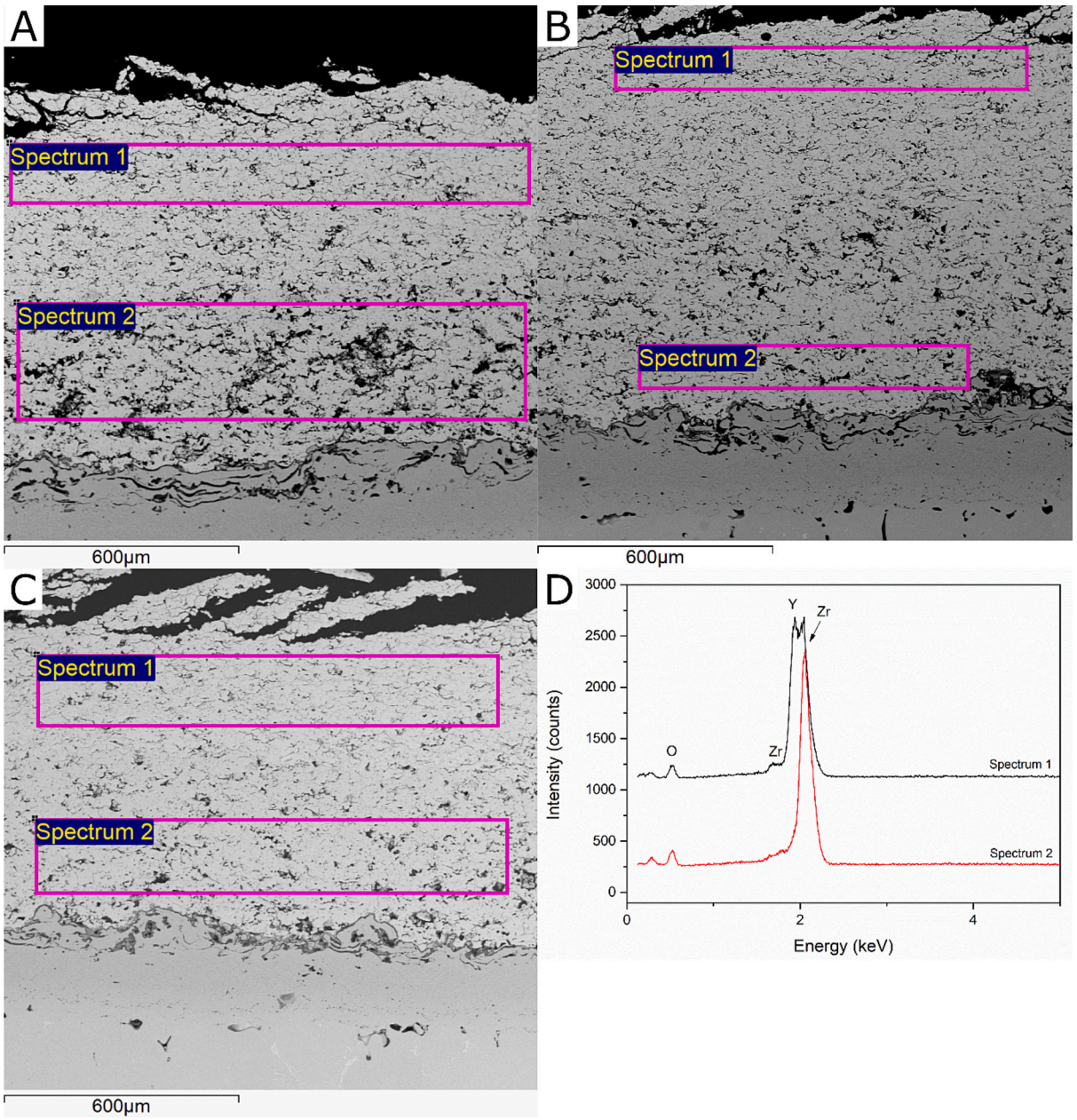

Fig. 25. EDX analysed areas: spectrum 1 acquired on the outer surface; spectrum 2 acquired on the inner surface of A) AAP-D (agglomerated and sintered feedstock); B) FFP-D (fused and crushed feedstock); C); HHP-D (HOSP feedstock) after CMAS corrosion testing.

using EDX revealed that below the infiltrated and chemically reacted "skin", the coating did not contain any elements related to the composition of CMAS (Fig. 25D). This indicates that the penetration of CMAS was limited to the outer surface only, probably because of the protective action of the silicate itself. It corroborates the assumption (laid out in the "Material and methods" section) that the thickness of the 55YSZ layer does not affect the outcome of this test, hence the choice of carrying it out only on the architecture of Fig. 1A. It also means that delamination of the CMAS-infiltrated "outer skin" of the 55YSZ layer likely did not happen during the isothermal contact period with molten CMAS. The yttrium-rich silicates would not have exerted a protective action if it did. By contrast, the interaction region spalled off during cooling, as the CMAS infiltrating the coating solidified and stiffened the system, so that the stresses due to thermal expansion mismatch resulted in crack propagation.

This finding is of great relevance as it indicates effective control over the penetration of CMAS by using an alternative material to 7-8YSZ as a top coat. It also means that, after the CMAS-infiltrated skin is peeled off during cooling, the remaining, unaffected 55YSZ layer can provide further protection during subsequent operational cycles, thus enabling safe long-term service.

Detailed image analysis was performed on SEM micrographs of the outer, reacted portion of the coatings to understand the CMAS penetration behaviour thoroughly and assess the impact of powder morphologies on the CMAS corrosion resistance of 55YSZ (Fig. 26).

The original SEM micrographs (Fig. 26A, C, E) of all samples and the respective analysed ones (Fig. 26B, D, F) are reported. The penetration of the CMAS melt was highlighted in red to compare the CMAS corrosion resistance of the bi-layer coatings obtained by the deposition with different powder morphologies. Within the analysed portion, it was observed that the AAP-A (Fig. 26A, B) and HHP-A (Fig. 26E, F) coatings exhibited a higher degree of CMAS penetration, with respectively ~19 % and ~ 15 % of the cross-sectional area being occupied by CMAS and/or by the yttrium-silicate reaction product. On the other hand, in the case

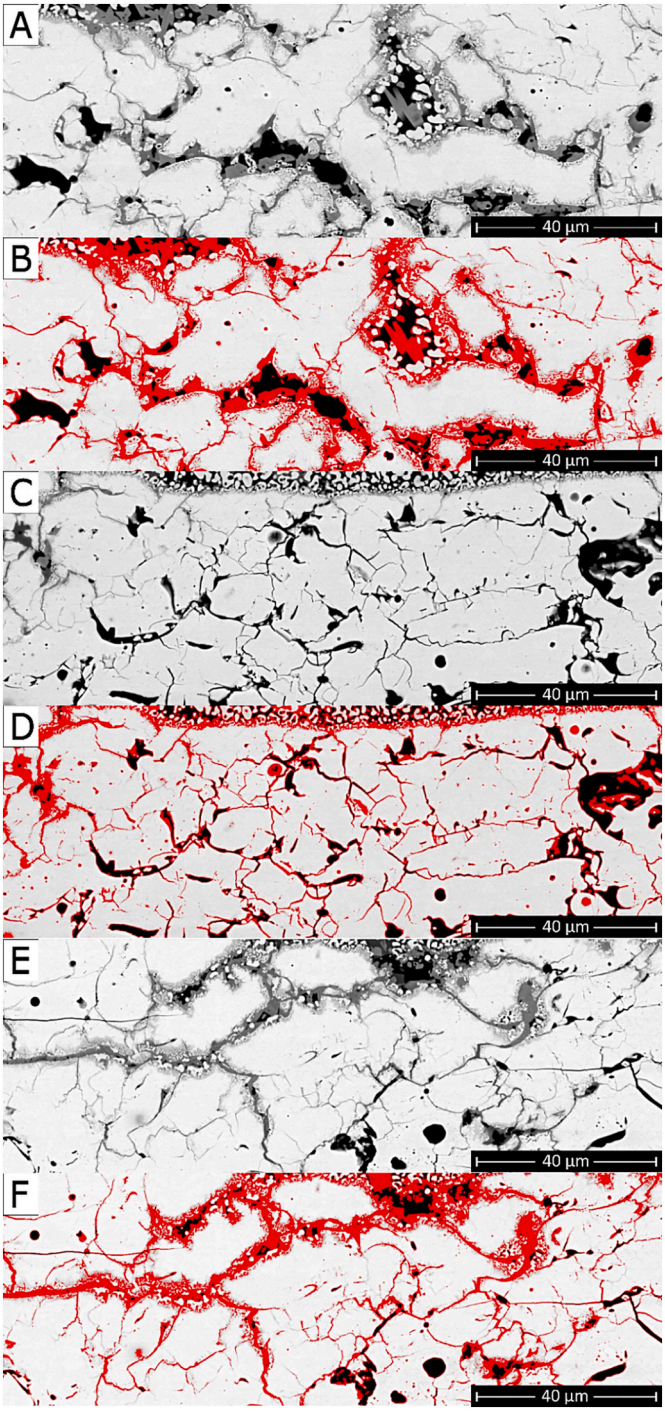

Fig. 26. SEM micrographs of the CMAS-corroded outer "skin" of the 55YSZ top layers: A,B) AAP-A (agglomerated and sintered feedstock); C,D) FFP-A (fused and crushed feedstock); E,F) HHP-A (HOSP feedstock). Panels A, C, E show the original SEM micrograph; panels B, D, F show the identification of CMAS and the yttrium-rich silicate reaction product by image analysis (highlighted in red colour).

of FFP-A (Fig. 26C, D), only ~12 % of the cross-sectional surface was occupied by CMAS and its reaction product. Once again, the samples obtained using the HOSP and A&S powders experienced a more significant attack than due to the more numerous intersplat boundaries and the presence of residual, fine-scale inner porosity, respectively.

3.2.5. *Thermal cycling resistance*

After pointing out that bi-layer systems using a 55YSZ outer layer with limited porosity can be effective in terms of CMAS resistance, the design of bi-layer systems with different total thickness and thickness ratios (Fig. 1) was undertaken to investigate the effect on thermal cycling performances. Thermal cycling failure of a TBC depends of several factors such as the difference in thermal expansion coefficients (CTE) between the various layers, the growth of the TGO and the thickness of each layer [61,62]. Through thermal cycling tests, it was observed that bi-layer systems (AAP-A, FFP-A, and HHP-A) with a combined thickness of 800 µm displayed a notable susceptibility to thermal shock. These systems tended to experience premature failure after undergoing only a limited number of cycles compared to bi-layer systems with lower total thickness but identical, 1:1 layer thickness

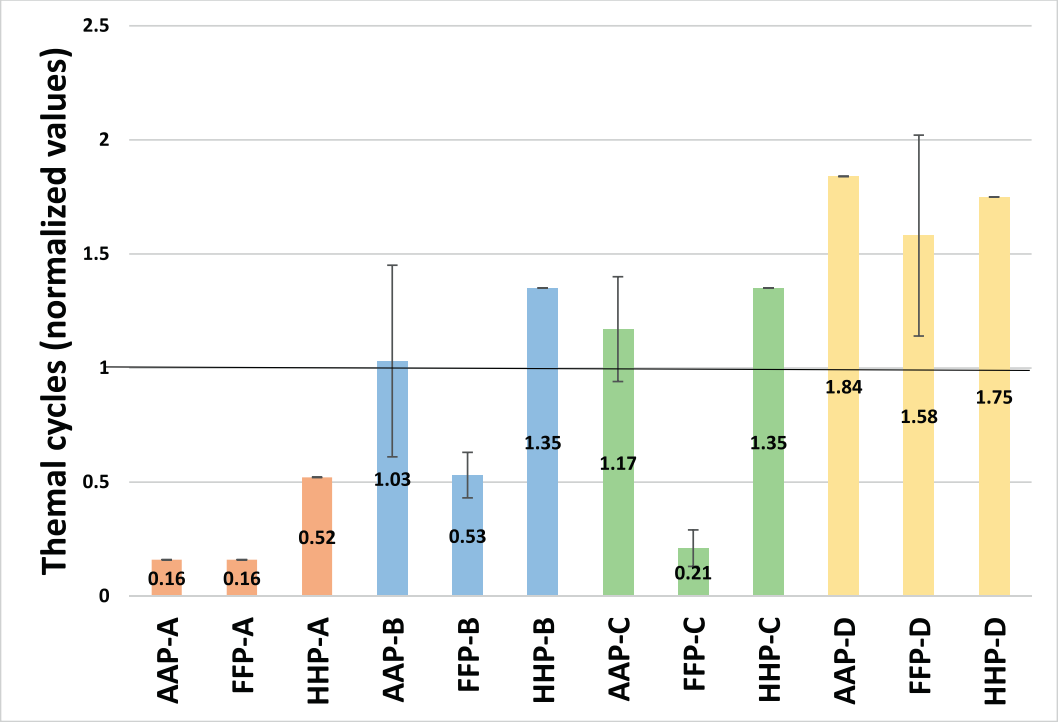

Fig. 27. Normalized number of thermal cycles to failure for all bi-layer coatings with different architectures.

ratio (AAP-B, FFP-B and HHP-B).

Keeping the total thickness fixed at 600 μm, a further improvement in thermal cycling resistance is obtained by increasing the thickness of the tougher 7-8YSZ bottom layer with respect to the more brittle 55YSZ top layer. Namely, the systems with a 250 μm-thick 55YSZ top layer and a 350 μm-thick 7-8YSZ bottom layer, designated as AAP-D, FFP-D, and HHP-D, exhibited the best TCF performance among the bi-layer samples (Fig. 27). To the contrary, an increase in the thickness of the 55YSZ top layer with respect to the 7-8YSZ bottom layer causes a slight but systematic drop in thermal cycling fatigue resistance irrespective of the powder manufacturing route (samples designated as AAP-C, FFP-C, and HHP-C in Fig. 27).

These results can be explained by analyzing the failure locations (Fig. 28). In the case of sample AAP-A, thermal cycling failure primarily took place at the coating edges, starting from the 55YSZ outer layer and propagating toward the interior (Fig. 28B). In the center of the sample, the coating thickness remained at 800 μm after the thermal cycling test. In samples FFP-A and HHP-A, the thermal cycling test resulted in the peeling of the 55YSZ layer even in the central region, leaving only 470 μm and 460 μm, respectively, attached to the substrate (Fig. 28C and E).

Thus, the main source of failure is the 55YSZ layer. This is understood, on the one hand, because this layer is notably more brittle than the 7-8YSZ bottom layer, as shown by the pillar-splitting results in Table 7. On the other hand, although the exact CTE value of 55YSZ composition is unavailable, the research conducted by Hayashi et al. demonstrated that the thermal expansion coefficient of YSZ decreases as the Y_2O_3 content increases [63]. Thus, the thermal expansion coefficient of 55YSZ is expected to be lower to that of 7YSZ CTE.

As a result, incorporating a thinner layer of 55YSZ (through a lower overall thickness and a comparatively thicker 7-8YZ bottom layer) has the potential to extend the overall durability of the system because it significantly:

(1) It reduces the overall stresses on the system because of the CTE mismatch during the cooling stage.

(2) It results in a greater fraction of the coating consisting of a tougher material with greater ability to tolerate stresses without crack propagation. Considering that the 7-8YSZ layer is not only made of an intrinsically tougher material but also more porous (hence more compliant), the benefit is twofold.

Notably, in the bi-layer coatings with the D architecture, which provided longer thermal cycling lifetime, delamination was shifted from the top layer to the interface between the TGO and the bottom 7-8YSZ layer (Fig. 29). Specifically, complete delamination was observed in the FFP-D system (Fig. 29B). SEM micrographs of AAP-D and HHP-D coatings revealed that crack initiation occurred at the interface between the TGO and the bottom 7-8YSZ layer (Fig. 29A, C) but did not progress to the same extent as in the FFP-D samples.

Interestingly, by measuring the TGO thickness in bi-layer coatings with both “A” and “D” architectures (Table 8), it was observed that the TGO thickness in architecture “A” was always <5 μm. In contrast, in architecture “D”, it exceeded 5 μm. The variation in TGO thickness can be attributed to the increased number of thermal cycles experienced by the coatings with architecture “D”. Consequently, it may explain the different cracking locations between the two architectures [13]. Specifically, premature failure in the 55YSZ layer with architecture “A” did not let the TGO grow thick enough to initiate interface delamination cracks as are seen with architecture “D”, and in the monolayer coatings analysed previously.

Concerning the powder morphologies, the coatings obtained by the F&C powders failed earlier than those obtained with the other feedstock powders in systems “B”, “C” and “D” (although the latter tests showed a considerable data scatter). This result mimics that seen with monolayer coating, and it can once again be explained by the lower porosity (hence, lower compliance) of the samples obtained with the F&C powder (Table 6). On the other hand, once again, the presence of intra-lamellar porosity and intersplat boundaries in the coatings obtained with the A&S and HOSP powders (respectively) helped tolerate thermal stresses arising from the thermal mismatch of the layers. The only partial exception is given by system “A”, where there was no significant

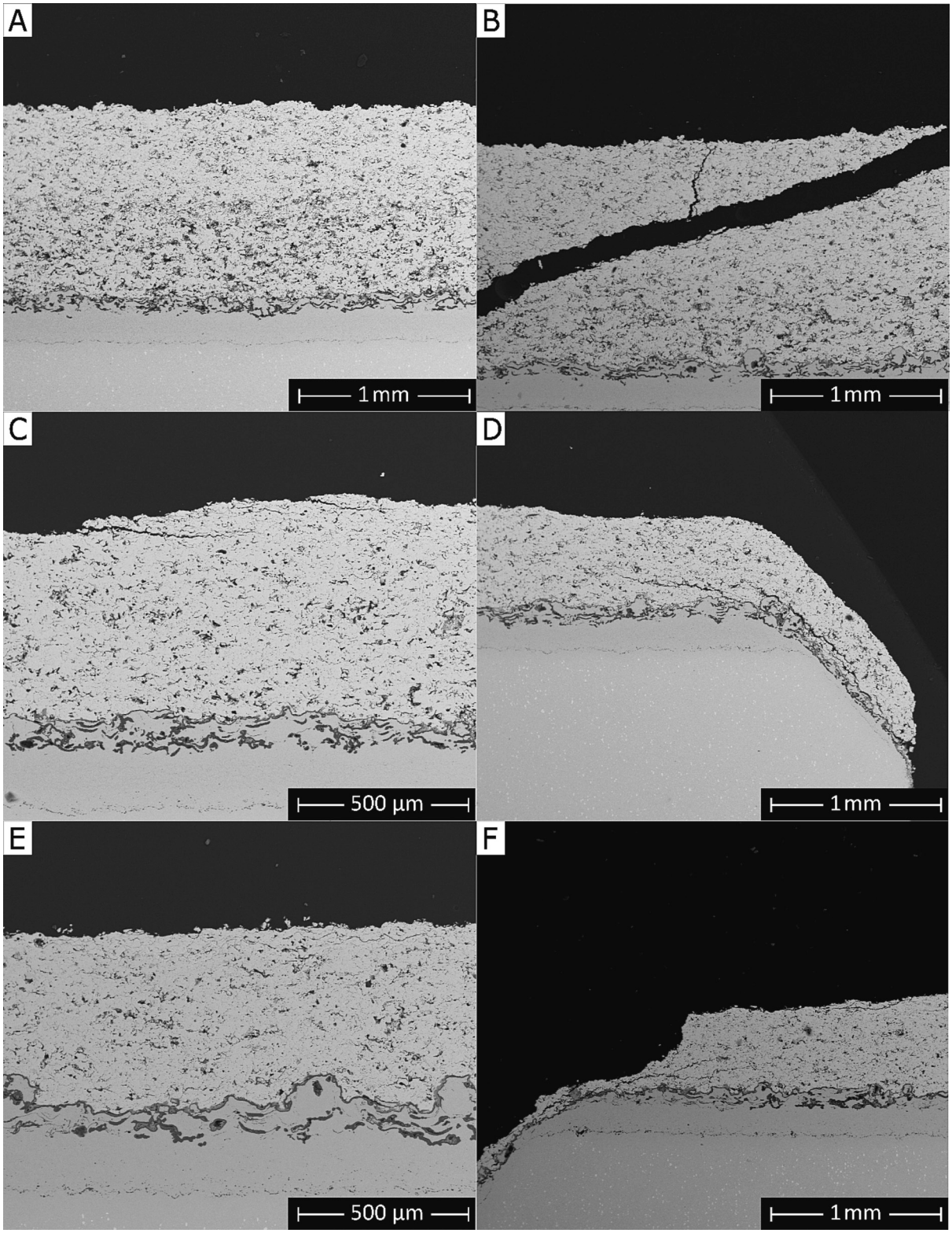

Fig. 28. BSE-SEM micrographs of thermal cycled bi-layer coating with A architecture (400–400 µm): A) AAP-A (agglomerated and sintered feedstock); B) edges of AAP-A; C) FFP-A (fused and crushed feedstock); D) edges of FFP-A; E) HHP-A (HOSP feedstock); F) edges of HHP-A.

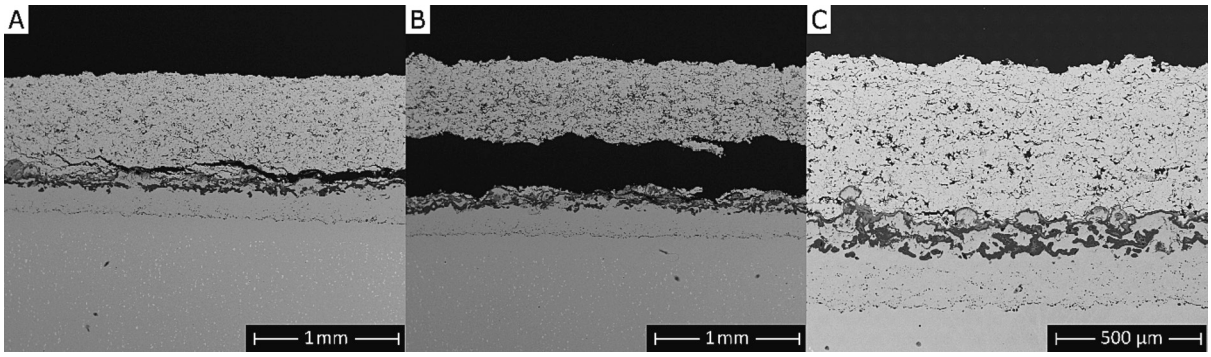

Fig. 29. BSE-SEM micrographs of thermal cycled bi-layer coatings with "D" architecture (250–350 µm): A) AAP-D; B) FFP-D; C) HHP-D.

Table 8
Thickness values of both bi-layer coatings with A and D architecture.

Sample	Thickness of TGO
AAP-A	2.77 ± 0.35
FFP-A	3.56 ± 0.28
HHP-A	3.81 ± 0.50
AAP-D	6.37 ± 1.69
FFP-D	6.49 ± 0.80
HHP-D	7.22 ± 0.79

difference between the AAP-A and FFP-A samples. System "A", however, experienced extremely early failure due to the very large CTE mismatch stresses and the great brittleness of the thick top layer; hence, the comparison between the effects of different feedstock powders might be less significant in this case.

4. Conclusions

In this work, 7-8YSZ monolayer coatings with both porous and dense vertically cracked (DVC) microstructures were produced using three different feedstock powder morphologies: porous Agglomerated and Sintered (A&S) granules, Hollow Spherical (HOSP) powders, and dense, irregular Fused and Crushed (F&C) particles.

Bi-layer coatings consisting of a 7-8YSZ bottom layer and a 55YSZ top layer were subsequently produced using the three feedstock powder types and changing the system architecture.

The following conclusions can be made concerning the 7-8YSZ monolayers:

- F&C powders yielded denser coatings than did the other powder types. This was particularly evident with the DVC coatings but also with the porous coatings.
- Both the porous and the DVC monolayer coatings demonstrated similar trends in terms of tensile adhesion/cohesion strength as a function of the powder manufacturing route. Still, every DVC coating showed $\sim$ 1.5 times higher tensile strength compared with the corresponding porous coating. Failure was adhesive in all porous coatings, due to the relatively limited extension of the real area of contact. Among the DVC samples, failure was adhesive with the F&C powder but cohesive or mixed with the A&S and HOSP powders, due to defects (inner porosity, interlamellar interfaces) in the layers.
- The coatings obtained sing the F&C powders, especially the DVC one, seem more effective in reducing the penetration of a CMAS melt. This is primarily attributed to the higher coating density.
- Regarding thermal cycling resistance, porous microstructures exhibit excellent resistance regardless of the powder used. Differently, DVC coatings showed a strong dependence on the feedstock powder. The F&C powder resulted in poorer thermal cycling performance, even if way above the target requested, as the denser coating was likely elastically stiffer.

Regarding the bi-layer coatings, the following considerations can be made:

- The "intrinsic" fracture toughness of 55YSZ measured by pillar splitting ($\sim$1.4 MPa$\bullet\sqrt{m}$) is lower than that of 7-8YSZ ($\sim$2.2 MPa$\bullet\sqrt{m}$).
- Tensile test failure occurred at the interface between the 7-8YSZ and 55YSZ layer regardless the powder manufacturing, and no intra-layer failure was detected.
- Bi-layer coatings with a 55YSZ top coat demonstrated higher CMAS resistance compared to 7-8YSZ monolayer coatings. CMAS penetration was limited to a few tens of microns of the top coat, causing its peeling due to cold shock during cooling. Denser top coats obtained with the F&C powder provided particularly good resistance.
- The TCF lifetime of bi-layer coatings strongly depended on the overall thickness and layer thickness ratio. The architecture with a reduced thickness of the brittle top layer (55YSZ) improved the durability of the TBC. On the other hand, using the F&C powder usually had a negative effect, like with the monolayer samples, probably because of the greater elastic stiffness of the denser layers.

CRediT authorship contribution statement

Simone Bursich: Formal analysis, Investigation, Methodology, Visualization, Writing – original draft, Writing – review & editing. **Stefania Morelli:** Conceptualization, Formal analysis, Investigation, Methodology, Visualization, Writing – original draft, Writing – review & editing. **Giovanni Bolelli:** Conceptualization, Formal analysis, Investigation, Methodology, Supervision, Visualization, Writing – review & editing. **Greta Cavazzini:** Formal analysis, Investigation, Methodology. **Edoardo Rossi:** Formal analysis, Investigation, Methodology. **Francesco Gerardo Mecca:** Formal analysis, Investigation, Methodology. **Salvatore Petruzzi:** Formal analysis, Investigation, Methodology. **Edoardo Bemporad:** Conceptualization, Project administration, Supervision, Writing – review & editing. **Luca Lusvarghi:** Conceptualization, Project administration, Supervision, Writing – review & editing.

Declaration of competing interest

The authors declare that they have no known competing financial interests or personal relationships that could have appeared to influence the work reported in this paper.

Data availability

No data was used for the research described in the article.

References

[1] C.U. Hardwicke, Y.C. Lau, Advances in thermal spray coatings for gas turbines and energy generation: a review, J. Therm. Spray Technol. 22 (2013) 564–576, https://doi.org/10.1007/s11666-013-9904-0.

[2] S. Bose, in: Butterworth-Heinemann (Ed.), High Temperature Coatings, Elsevier, Oxford, United Kingdom, 2007, https://doi.org/10.1016/B978-0-7506-8252-7.X5000-8.

[3] J.C. Han, Gas turbine heat transfer and cooling technology, in: T.F. Inc (Ed.), Proc. Natl. Heat Transf. Conf., 2012, https://doi.org/10.1201/b13616. Pages.

[4] H.I.H. Saravanamuttoo, H. Cohen, G.F.C. Rogers, A.C. Nix, P.V. Straznicky, Gas Turbine Theory, Pearson, 2017, p. 606, 7th ed.

[5] N.P. Padture, M. Gell, E.H. Jordan, Thermal barrier coatings for gas-turbine engine applications, Science (80-.) 296 (2002) 280–284, https://doi.org/10.1126/science.1068609.

[6] W. Li, H. Zhao, X. Zhong, L. Wang, S. Tao, Air plasma-sprayed yttria and yttria-stabilized zirconia thermal barrier coatings subjected to calcium-magnesium-alumino-silicate (CMAS), J. Therm. Spray Technol. 23 (2014) 975–983, https://doi.org/10.1007/s11666-014-0107-0.

[7] J. Xia, L. Yang, R.T. Wu, Y.C. Zhou, L. Zhang, K.L. Huo, M. Gan, Degradation mechanisms of air plasma sprayed free-standing yttria-stabilized zirconia thermal barrier coatings exposed to volcanic ash, Appl. Surf. Sci. 481 (2019) 860–871, https://doi.org/10.1016/j.apsusc.2019.03.084.

[8] Z. Cai, J. Jiang, W. Wang, Y. Liu, Z. Cao, CMAS penetration-induced cracking behavior in the ceramic top coat of APS TBCs, Ceram. Int. 45 (2019) 14366–14375, https://doi.org/10.1016/j.ceramint.2019.04.152.

[9] R. Vassen, X. Cao, F. Tietz, D. Basu, D. Sto, Zirconates as new materials for thermal barrier coatings, J. Am. Ceram. Soc. 83 (2004) 2023–2028, https://doi.org/10.1111/j.1151-2916.2000.tb01506.x.

[10] L. Cai, W. Ma, B. Ma, F. Guo, W. Chen, H. Dong, Y. Shuang, Air plasma-sprayed $La_2Zr_2O_7SrZrO_3$ composite thermal barrier coating subjected to CaO-MgO-Al_2O_3-SiO_2 (CMAS), J. Therm. Spray Technol. 26 (2017) 1076–1083, https://doi.org/10.1007/s11666-017-0587-9.

[11] M. Li, Y. Cheng, L. Guo, Y. Zhang, C. Zhang, S. He, W. Sun, F. Ye, Preparation of nanostructured $Gd_2Zr_2O_7$-$LaPO_4$ thermal barrier coatings and their calcium-magnesium-alumina-silicate (CMAS) resistance, J. Eur. Ceram. Soc. 37 (2017) 3425–3434, https://doi.org/10.1016/j.jeurceramsoc.2017.03.069.

[12] H. Fang, W. Wang, J. Huang, Y. Li, D. Ye, Corrosion behavior and thermos-physical properties of a promising Yb_2O_3 and Y_2O_3 co-stabilized ZrO_2 ceramic for thermal barrier coatings subject to calcium-magnesium-aluminum-silicate (CMAS) depositio, Corros. Sci. 182 (2021), https://doi.org/10.1016/j.corsci.2020.109230.

[13] V. Viswanathan, G. Dwivedi, S. Sampath, Multilayer, multimaterial thermal barrier coating systems: design, synthesis, and performance assessment, J. Am. Ceram. Soc. 98 (2015) 1769–1777, https://doi.org/10.1111/jace.13563.

[14] S. Mahade, D. Zhou, N. Curry, N. Markocsan, P. Nylén, R. Vaßen, Tailored microstructures of gadolinium zirconate/YSZ multi-layered thermal barrier coatings produced by suspension plasma spray: durability and erosion testing, J. Mater. Process. Technol. 264 (2019) 283–294, https://doi.org/10.1016/j.jmatprotec.2018.09.016.

[15] P.G. Lashmi, P.V. Ananthapadmanabhan, G. Unnikrishnan, S.T. Aruna, Present status and future prospects of plasma sprayed multilayered thermal barrier coating systems, J. Eur. Ceram. Soc. 40 (2020) 2731–2745, https://doi.org/10.1016/j.jeurceramsoc.2020.03.016.

[16] J.L. Smialek, R.A. Miller, Revisiting the birth of 7YSZ thermal barrier coatings: Stephan stecura, Coatings 8 (2018) 7–12, https://doi.org/10.3390/coatings8070255.

[17] S. Morelli, S. Bursich, V. Testa, G. Bolelli, A. Miccichè, L. Lusvarghi, CMAS corrosion and thermal cycling fatigue resistance of alternative thermal barrier coating materials and architectures: a comparative evaluation, Surf. Coat. Technol. 439 (2022), https://doi.org/10.1016/j.surfcoat.2022.128433.

[18] J.J. Gomez Chavez, R. Naraparaju, P. Mechnich, K. Kelm, U. Schulz, C.V. Ramana, Effects of yttria content on the CMAS infiltration resistance of yttria stabilized thermal barrier coatings system, J. Mater. Sci. Technol. 43 (2020) 74–83, https://doi.org/10.1016/j.jmst.2019.09.039.

[19] M. Ahrens, R. Vaßen, D. Stöver, Stress distributions in plasma-sprayed thermal barrier coatings as a function of interface roughness and oxide scale thickness, Surf. Coat. Technol. 161 (2002) 26–35, https://doi.org/10.1016/S0257-8972(02)00359-6.

[20] X. Song, M. Xie, F. Zhou, G. Jia, X. Hao, S. An, High-temperature thermal properties of yttria fully stabilized zirconia ceramics, J. Rare Earths 29 (2011) 155–159, https://doi.org/10.1016/S1002-0721(10)60422-X.

[21] K.J. Nicholls, J.R. Lawson, Methods to reduce the thermal conductivity of EB-PVD TBC's, Surf. Coat. Technol. 151–152 (2002) 383–391.

[22] S. Krämer, J. Yang, C.G. Levi, C.A. Johnson, Thermochemical interaction of thermal barrier coatings with molten CaO-MgO-Al_2O_3-SiO_2 (CMAS) deposits, J. Am. Ceram. Soc. 89 (2006) 3167–3175, https://doi.org/10.1111/j.1551-2916.2006.01209.x.

[23] M.H. Vidal-Setif, N. Chellah, C. Rio, C. Sanchez, O. Lavigne, Calcium-magnesium-alumino-silicate (CMAS) degradation of EB-PVD thermal barrier coatings: characterization of CMAS damage on ex-service high pressure blade TBCs, Surf. Coat. Technol. 208 (2012) 39–45, https://doi.org/10.1016/j.surfcoat.2012.07.074.

[24] L. Łatka, Thermal barrier coatings manufactured by suspension plasma spraying - a review, Adv. Mater. Sci. 18 (2018) 95–117, https://doi.org/10.1515/adms-2017-0044.

[25] N. Curry, K. VanEvery, T. Snyder, J. Susnjar, S. Bjorklund, Performance testing of suspension plasma sprayed thermal barrier coatings produced with varied suspension parameters, Coatings 5 (2015) 338–356, https://doi.org/10.3390/coatings5030338.

[26] S.V. Shinde, E.J. Gildersleeve, V.C.A. Johnson, S. Sampath, Segmentation crack formation dynamics during air plasma spraying of zirconia, Acta Mater. 183 (2020) 196–206, https://doi.org/10.1016/j.actamat.2019.10.052.

[27] A. Nouri, A. Sola, Powder morphology in thermal spraying, J. Adv. Manuf. Process. 1 (2019) 1–19, https://doi.org/10.1002/amp2.10020.

[28] S. Sampath, U. Schulz, M.O. Jarligo, S. Kuroda, Processing science of advanced thermal-barrier systems, MRS Bull. 37 (2012) 903–910, https://doi.org/10.1557/mrs.2012.233.

[29] P.K. Mehrotra, Powder processing and green shaping, Compr. Hard Mater. 1 (2014) 213–235, https://doi.org/10.1016/B978-0-08-096527-7.00007-6.

[30] R.M. German, Consolidation Techniques, Compr. Hard Mater. 1 (2014) 237–263, https://doi.org/10.1016/B978-0-08-096527-7.00008-8.

[31] O.P. Solonenko, I.P. Gulyaev, A.V. Smirnov, Thermal plasma processes for production of hollow spherical powders: theory and experiment, J. Therm. Sci. Technol. 6 (2011) 219–234, https://doi.org/10.1299/jtst.6.219.

[32] A.J. Allen, G.G. Long, H. Boukari, J. Ilavsky, A. Kulkarni, S. Sampath, H. Herman, A.N. Goland, Microstructural characterization studies to relate the properties of thermal-spray coatings to feedstock and spray conditions, Surf. Coat. Technol. 146–147 (2001) 544–552, https://doi.org/10.1016/S0257-8972(01)01433-5.

[33] G. Bertrand, P. Bertrand, P. Roy, C. Rio, R. Mevrel, Low conductivity plasma sprayed thermal barrier coating using hollow psz spheres: correlation between thermophysical properties and microstructure, Surf. Coat. Technol. 202 (2008) 1994–2001, https://doi.org/10.1016/j.surfcoat.2007.08.042.

[34] W. Chi, S. Sampath, H. Wang, Microstructure-thermal conductivity relationships for plasma-sprayed yttria-stabilized zirconia coatings, J. Am. Ceram. Soc. 91 (2008) 2636–2645, https://doi.org/10.1111/j.1551-2916.2008.02476.x.

[35] Z. Wang, A. Kulkarni, S. Deshpande, T. Nakamura, H. Herman, Effects of pores and interfaces on effective properties of plasma sprayed zirconia coatings, Acta Mater. 51 (2003) 5319–5334, https://doi.org/10.1016/S1359-6454(03)00390-2.

[36] G. Bolelli, M.G. Righi, M.Z. Mughal, R. Moscatelli, O. Ligabue, N. Antolotti, M. Sebastiani, L. Lusvarghi, E. Bemporad, Damage progression in thermal barrier coating systems during thermal cycling: a nano-mechanical assessment, Mater. Des. 166 (2019), https://doi.org/10.1016/j.matdes.2019.107615.

[37] B. Vignesh, W.C. Oliver, G.S. Kumar, P.S. Phani, Critical assessment of high speed nanoindentation mapping technique and data deconvolution on thermal barrier coatings, Mater. Des. 181 (2019), 108084, https://doi.org/10.1016/j.matdes.2019.108084.

[38] M. Sebastiani, K.E. Johanns, E.G. Herbert, F. Carassiti, G.M. Pharr, A novel pillar indentation splitting test for measuring fracture toughness of thin ceramic coatings, Philos. Mag. 95 (2015) 1928–1944, https://doi.org/10.1080/14786435.2014.913110.

[39] R.S. Lima, Perspectives on thermal gradients in porous ZrO_2-7–8 wt.% Y_2O_3 (YSZ) thermal barrier coatings (TBCs) manufactured by air plasma spray (APS), Coatings 10 (2020) 1–18, https://doi.org/10.3390/coatings10090812 (License CC BY 4.0).

[40] N. Curry, M. Leitner, K. Körner, High-porosity thermal barrier coatings from high-power plasma spray equipment—processing, performance and economics, Coatings 10 (2020) 1–25, https://doi.org/10.3390/coatings10100957.

[41] W.C. Oliver, G.M. Pharr, An improved technique for determining hardness and elastic madulus using load and displacement, J. Mater. Res. 7 (1992) 1564–1583, https://doi.org/10.1557/JMR.1992.1564.

[42] M. Sebastiani, R. Moscatelli, F. Ridi, P. Baglioni, F. Carassiti, High-resolution high-speed nanoindentation mapping of cement pastes: unravelling the effect of microstructure on the mechanical properties of hydrated phases, Mater. Des. 97 (2016) 372–380, https://doi.org/10.1016/j.matdes.2016.02.087.

[43] H. Besharatloo, J.M. Wheeler, Influence of indentation size and spacing on statistical phase analysis via high-speed nanoindentation mapping of metal alloys, J. Mater. Res. 36 (2021) 2198–2212, https://doi.org/10.1557/s43578-021-00214-5.

[44] P. Sudharshan Phani, W.C. Oliver, A critical assessment of the effect of indentation spacing on the measurement of hardness and modulus using instrumented indentation testing, Mater. Des. 164 (2019), 107563, https://doi.org/10.1016/j.matdes.2018.107563.

[45] C.M. Lauener, L. Petho, M. Chen, Y. Xiao, J. Michler, J.M. Wheeler, Fracture of silicon: influence of rate, positioning accuracy, FIB machining, and elevated temperatures on toughness measured by pillar indentation splitting, Mater. Des. 142 (2018) 340–349, https://doi.org/10.1016/j.matdes.2018.01.015.

[46] M. Ghidelli, M. Sebastiani, K.E. Johanns, G.M. Pharr, Effects of indenter angle on micro-scale fracture toughness measurement by pillar splitting, J. Am. Ceram. Soc. 100 (2017) 5731–5738, https://doi.org/10.1111/jace.15093.

[47] H. Guo, S. Kuroda, H. Murakami, Microstructures and properties of plasma-sprayed segmented thermal barrier coatings, J. Am. Ceram. Soc. 89 (2006) 1432–1439, https://doi.org/10.1111/j.1551-2916.2005.00912.x.

[48] S. Morelli, V. Testa, G. Bolelli, O. Ligabue, E. Molinari, N. Antolotti, L. Lusvarghi, CMAS corrosion of YSZ thermal barrier coatings obtained by different thermal spray processes, J. Eur. Ceram. Soc. 40 (2020) 4084–4100, https://doi.org/10.1016/j.jeurceramsoc.2020.04.058.

[49] J.A. Krogstad, S. Krämer, D.M. Lipkin, C.A. Johnson, D.R.G. Mitchell, J.M. Cairney, C.G. Levi, Phase stability of t'-zirconia-based thermal barrier coatings: mechanistic insights, J. Am. Ceram. Soc. 94 (2011) 168–177, https://doi.org/10.1111/j.1551-2916.2011.04531.x.

[50] A. Nieto, M. Walock, Calcia-magnesia-alumina-silicate (CMAS) infiltration behavior in high temperature ceramics and coatings, In: 2018 Jt. Propuls. Conf., 2018: pp. 1–12. doi:https://doi.org/10.2514/6.2018-4833.
[51] C. Mercer, S. Faulhaber, A.G. Evans, R. Darolia, A delamination mechanism for thermal barrier coatings subject to calcium-magnesium-alumino-silicate (CMAS) infiltration, Acta Mater. 53 (2005) 1029–1039, https://doi.org/10.1016/j.actamat.2004.11.028.
[52] H. Dong, G.J. Yang, C.X. Li, X.T. Luo, C.J. Li, Effect of TGO thickness on thermal cyclic lifetime and failure mode of plasma-sprayed TBCs, J. Am. Ceram. Soc. 97 (2014) 1226–1232, https://doi.org/10.1111/jace.12868.
[53] M. Jinnestrand, S. Sjöström, Investigation by 3D FE simulations of delamination crack initiation in TBC caused by alumina growth, Surf. Coat. Technol. 135 (2001) 188–195, https://doi.org/10.1016/S0257-8972(00)01084-7.
[54] M. Martena, D. Botto, P. Fino, S. Sabbadini, M.M. Gola, C. Badini, Modelling of TBC system failure: stress distribution as a function of TGO thickness and thermal expansion mismatch, Eng. Fail. Anal. 13 (2006) 409–426, https://doi.org/10.1016/j.engfailanal.2004.12.027.
[55] A. Rabiei, A.G. Evans, Failure mechanisms associated with the thermally grown oxide in plasma-sprayed thermal barrier coatings, Acta Mater. 48 (2000) 3963–3976, https://doi.org/10.1016/S1359-6454(00)00171-3.
[56] A.J. Lockett, Performance analysis, in: Gen. Optim. Through Inf. Maximization, Springer, Berlin, 2020, pp. 239–262, https://doi.org/10.1007/978-3-662-62007-6_10.
[57] J. Chevalier, L. Gremillard, A.V. Virkar, D.R. Clarke, The tetragonal-monoclinic transformation in zirconia: lessons learned and future trends, J. Am. Ceram. Soc. 92 (2009) 1901–1920, https://doi.org/10.1111/j.1551-2916.2009.03278.x.
[58] C. Mercer, J.R. Williams, D.R. Clarke, A.G. Evans, On a ferroelastic mechanism governing the toughness of metastable tetragonal-prime (t') yttria-stabilized zirconia, Proc. R. Soc. A Math. Phys. Eng. Sci. 463 (2007) 1393–1408, https://doi.org/10.1098/rspa.2007.1829.
[59] A.R. Krause, B.S. Senturk, H.F. Garces, G. Dwivedi, A.L. Ortiz, S. Sampath, N. P. Padture, $2ZrO_2{\cdot}Y_2O_3$ thermal barrier coatings resistant to degradation by molten CMAS: part I, optical basicity considerations and processing, J. Am. Ceram. Soc. 97 (2014) 3943–3949, https://doi.org/10.1111/jace.13210.
[60] Z. Tian, J. Zhang, L. Zheng, W. Hu, X. Ren, Y. Lei, J. Wang, General trend on the phase stability and corrosion resistance of rare earth monosilicates to molten calcium–magnesium–alumino silicate at 1300 °C, Corros. Sci. 148 (2019) 281–292, https://doi.org/10.1016/j.corsci.2018.12.032.
[61] C.J. Li, H. Dong, H. Ding, G.J. Yang, C.X. Li, The correlation of the TBC lifetimes in burner cycling test with thermal gradient and furnace isothermal cycling test by TGO effects, J. Therm. Spray Technol. 26 (2017) 378–387, https://doi.org/10.1007/s11666-017-0530-0.
[62] D.R. Mumm, G.A. Evans, Mechanisms controlling the performance and durability of thermal barrier coatings, Key Eng. Mater. 197 (2001) 199–230, https://doi.org/10.4028/www.scientific.net/kem.197.199.
[63] H. Hayashi, T. Saitou, N. Maruyama, H. Inaba, K. Kawamura, M. Mori, Thermal expansion coefficient of yttria stabilized zirconia for various yttria contents, Solid State Ionics 176 (2005) 613–619, https://doi.org/10.1016/j.ssi.2004.08.021.